

© 2019 by Akshat Puri. All rights reserved.

MEASUREMENT OF ANGULAR AND MOMENTUM DISTRIBUTIONS OF CHARGED
PARTICLES WITHIN AND AROUND JETS IN Pb+Pb AND $p\bar{p}$ COLLISIONS AT
 $\sqrt{S_{NN}} = 5.02$ TeV WITH ATLAS AT THE LHC

BY

AKSHAT PURI

DISSERTATION

Submitted in partial fulfillment of the requirements
for the degree of Doctor of Philosophy in Physics
in the Graduate College of the
University of Illinois at Urbana-Champaign, 2019

Urbana, Illinois

Doctoral Committee:

Professor Matthias Grosse Perdekamp, Chair
Professor Anne Marie Sickles, Advisor
¹ Professor Lance Cooper
Professor Bryce Gadaway

Abstract

2 Heavy ion collision experiments have been centered around studying the extreme state of matter formed in
3 such collisions, the quark-gluon plasma. There have been efforts to measure and characterize this state of
4 matter for almost two decades, first at the Relativistic Heavy Ion Collider and subsequently at the Large
5 Hadron Collider. While there have been different approaches to study it, correlated particle showers called
6 jets have found a special place as a probe of the QGP. Arising from highly energetic collisions between
7 partons, jets are formed early enough in heavy ion collisions that they experience the formation of the QGP
8 and its evolution. They are modified from what they would be in a vacuum, and studying these modifications
9 can give insight into the properties of the QGP as well as the strong interaction.

10 Jet measurements can focus on a variety of observables like yields, momenta, or fragmentation patterns,
11 each with its own limitations and advantages. This thesis presents a measurement of the angular distribution
12 of charged particles around the jet axis as measured by the ATLAS detector for Pb+Pb and pp collisions
13 with a center of mass energy of $\sqrt{s_{NN}} = 5.02$ TeV. Comparing the measurement in the two systems shows
14 that charged particles carrying a transverse momenta p_T of less than 4 GeV have a broader distribution
15 in Pb+Pb collisions, while those with $p_T > 4$ GeV have a narrower distribution. Furthermore, there is an
16 enhancement for particles with $p_T < 4$ GeV in Pb+Pb collisions, with the enhancement increasing up to 2
17 for $r < 0.3$ from the jet axis, and remaining constant for $0.3 < r < 0.6$. Charged particles with $p_T > 4$ GeV
18 show a small enhancement in the jet core for $r < 0.05$, and are increasingly suppressed up to 0.5 for $r < 0.3$.
19 This depletion remains constant for $0.3 < r < 0.6$.

For my Mother, Father, and Brother

Contents

23	Chapter 1 Introduction	1
24	1.1 Quantum Chromodynamics	1
25	1.2 Quark-Gluon Plasma	4
26	1.3 Heavy Ion Collisions	8
27	1.4 Jets and Jet Quenching	13
28	1.4.1 Jets in e^+e^- collisions	13
29	1.4.2 Jets in pp collisions	14
30	1.4.3 Jets in heavy ion collisions	15
31	1.4.4 Jet Reconstruction	18
32	Chapter 2 Major Jet Measurements	21
33	2.1 Dijet Balance: x_J	21
34	2.2 Modification of jet yields: R_{AA}	22
35	2.3 Jet Fragmentation	25
36	2.4 Effective Quenching	28
37	2.5 Jet Fluid model	33
38	2.6 Hybrid Model	36

Chapter 1

Introduction

39 This section shall discuss the theoretical background necessary to understand jet measurements. It will
40 discuss the fundamentals of quantum chromodynamics (QCD), the quark gluon plasma and the heavy ion
41 collision system it is formed in, and finally jets and jet energy loss.
42 remove Refs. [1].

43 1.1 Quantum Chromodynamics

44 Quantum Chromodynamics is a gauge theory with SU(3) symmetry that describes the dynamics of the strong
45 interactions between quarks and gluons. It is part of the Standard Model [2], the building blocks of which
46 are shown in Figure 1.1.

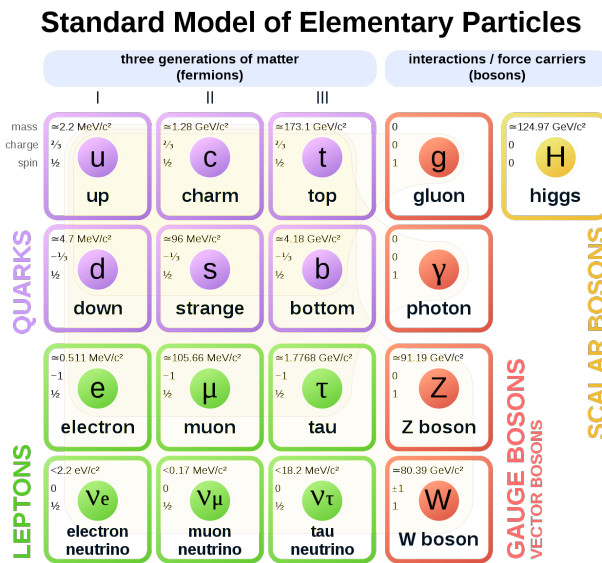


Figure 1.1: The elementary particles of the standard model. Figure taken from Ref. [3].

47 Quarks are fermions with a spin of $1/2$, and carry a fractional electric charge as well as a color charge.

48 They all have mass and come in six flavors: up, down, strange, charm, top, bottom. The lightest quarks
 49 (u and d) combine and form stable particles, while the heavier quarks can only be produced in energetic
 50 environments and decay rapidly. Gluons are gauge bosons (force carriers) with a spin of 1, and are what hold
 51 quarks together. The dynamics of the quarks and gluons, collectively referred to as partons are described by
 52 the QCD Lagrangian given by [4]:

$$\mathcal{L}_{\text{QCD}} = \sum_q \bar{\psi}_{q,a} (i\gamma^\mu \partial_\mu \delta_{ab} - g_s \gamma^\mu t_{ab}^C \mathcal{A}_\mu^C - m_q \delta_{ab}) \psi_{q,b} - \frac{1}{4} F_{\mu\nu}^A F^{A\mu\nu} \quad (1.1)$$

53 where $\psi_{q,a}$ and $\psi_{q,b}$ are quark-field spinors for a quarks with flavor q , mass m_q , and color a and b respectively,
 54 with the values for a and b ranging from 1 to 3 (for the three colors). The \mathcal{A}_μ^C corresponds to the gluon field
 55 with C taking values from 1 through 8 (for the 8 types of gluons). The t_{ab}^C corresponds to the Gell-Mann
 56 matrices that are the generators of the SU(3) group, and dictate the rotation of the quarks color in SU(3)
 57 space when it interacts with a gluon. The coupling constant is encoded within g_s , which is defined by
 58 $g_s \equiv \sqrt{4\pi\alpha_s}$. The field tensor $F_{\mu\nu}^A$ can be written in terms of the structure constants of the SU(3) group
 59 f_{ABC} , and is given by:

$$F_{\mu\nu}^A = \partial_\mu \mathcal{A}_\nu^A - \partial_\nu \mathcal{A}_\mu^A - g_s f_{ABC} \mathcal{A}^B \mathcal{A}^C \quad (1.2)$$

60 While many parallels can be drawn between Quantum Electrodynamics (QED, the theory that describes
 61 photons and electrons) and QCD, the main difference between the two comes from the gluon-gluon interactions
 62 allowed in QCD, making it non-Abelian. These interactions can be summarized as shown in Figure 1.2.

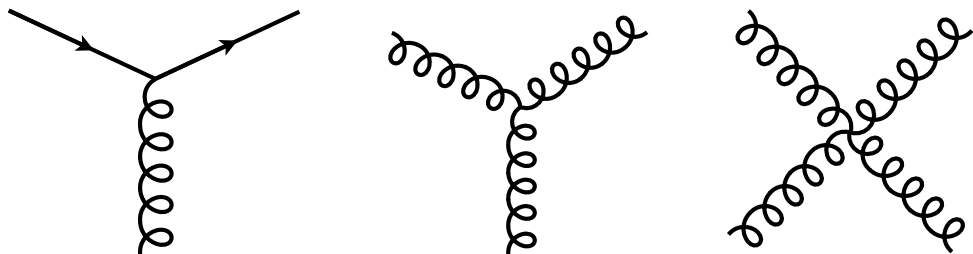


Figure 1.2: The allowed vertices in QCD. The vertices involving two or more gluons are unique to QCD and do not have a QED analog.

63 A core feature of QCD is that the coupling constant α_s has an energy dependence shown in Figure 1.3.

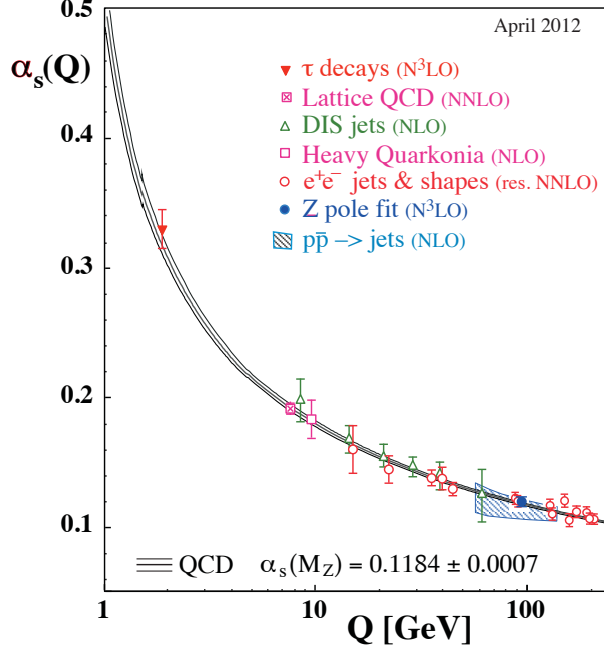


Figure 1.3: The running coupling constant α_s as a function of the momentum transfer Q . Figure taken from Ref. [4].

64 This dependence can be expressed in terms of the β function as

$$Q^2 \frac{\partial \alpha_s(Q^2)}{\partial Q^2} = \beta(\alpha_s(Q^2)) \quad (1.3)$$

65 where Q is the momentum transfer in the particle reaction. The beta function can be expressed using
66 perturbative QCD (pQCD) as:

$$\beta(\alpha_s) = -(b_0 \alpha_s^2 + b_1 \alpha_s^3 + b_2 \alpha_s^4 \dots) \quad (1.4)$$

67 where the coefficients b_i depend on the number of colors and flavors. This running coupling constant is small
68 and asymptotically tends to zero at large energy scales (or at small distances) and is large at small energy
69 scales (large distances). This running coupling phenomenon leads to two key behaviors: asymptotic freedom
70 and color confinement.

71 **Asymptotic Freedom:** At high energy scales (small distances), the QCD coupling constant α_s is
 72 small and tends to zero, implying a free particle behavior of quarks and gluons[5, 6]. This has been observed
 73 by a variety of deep inelastic scattering (DIS) experiments [7–20]. These scattering experiments shown in
 74 Figure 1.4, probe the interior of a nucleon using highly energetic leptons like electrons. The electron scatters
 75 off of the target proton, producing a lepton and a hadron shower. Bu First done by MIT-SLAC [21, 22],
 76 these DIS experiments showed the weak Q^2 dependence on the inelastic scattering cross-sections, as well as
 77 Bjorken scaling [23], where the proton structure functions are independent of the momentum transfer. These
 78 experiments revealed the point-like constituents of the proton and paved the road to an asymptotically free
 79 theory.

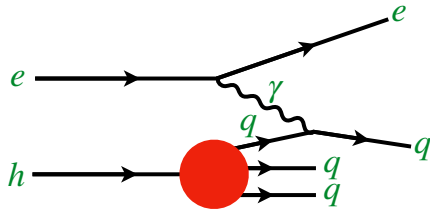


Figure 1.4: Schematic of the deep inelastic scattering experiment.

80 **Color Confinement** The opposite end of the running coupling constant phenomenon is color confinement.
 81 Proved to be a consequence of asymptotic freedom in Ref [24], this property of QCD described in
 82 Ref. [25] forbids the direct observation of free quarks and gluons, allowing only for composite particles that
 83 are color singlets. While have been numerous efforts to understand the source of this phenomenon like in
 84 Refs. [26–32], these are based on numerical calculations. An analytic proof of color confinement still escapes
 85 description and in fact, is one of the Millennium Problems [33].

86 1.2 Quark-Gluon Plasma

87 The quark-gluon plasma is a state of matter that comprises of free partons and is formed in extreme conditions
 88 of temperature and pressure [34]. Its study is motivated by the fact that is the only way to access the
 89 dynamics of partons that are otherwise confined within hadrons. Moreover, its thermodynamic properties are
 90 of particular interest since it filled the early universe a few microseconds after the Big Bang [35]. The QGP
 91 also forms the core of neutron-stars [36] and the recent detection of gravitational waves from a neutron-star
 92 merger [37] has opened new avenues of investigation [38–40]. These studies have the potential to provide
 93 information into the nuclear equation of state since the dynamics of the merger are sensitive to the behavior

94 of extremely dense nuclear matter [41]. The increase in temperatures and density during the merger results
 95 in different pre- and post-merger signals of gravitational-waves that suggest a signature of a first-order
 96 hadron-quark phase transition at extreme densities [42]. Colliders like RHIC and the LHC on the other
 97 hand probe regions that have comparatively low baryon densities. Lattice QCD calculations in these regions
 98 show that the transition between a hadronic gas and the QGP occurs at a temperature of approximately 160
 99 MeV and corresponds to an energy density of 0.5 GeV/fm^3 [43]. This is a smooth crossover that spans a
 100 20–30 MeV temperature range, and can be seen in the QCD phase diagram shown in Figure 1.5. This phase
 101 diagram shows the transition between free quarks and gluons within the QGP and the confined quarks and
 102 gluons within hadrons, as a function of temperature T and baryon chemical potential μ .

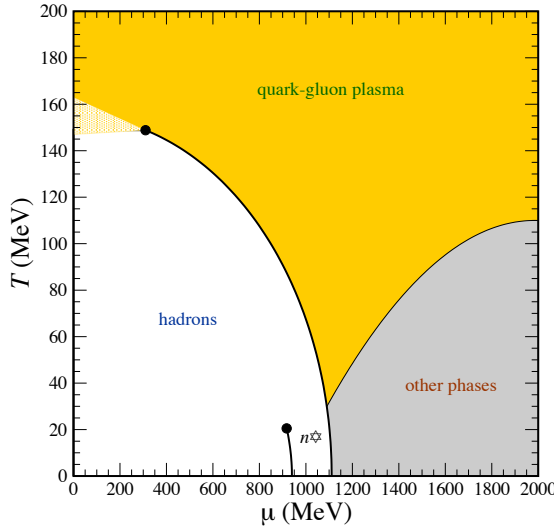


Figure 1.5: The QCD phase diagram of nuclear matter as a function of temperature T and baryon chemical potential μ . The $n\star$ denotes a neutron star. Figure from Ref. [44].

103 When formed in a heavy ion collision, this state of matter exists for 1–10 fm/c, depending on the collision
 104 energy [45]. Thermal photons from the QGP reveal that it reaches temperatures of 300–600 MeV in central
 105 collisions at 200 GeV [46] and 2.76 TeV [47], showing very little collision energy dependence. As the QGP
 106 cools via expansion, its temperature drops below the critical temperature of QCD phase transitions and it
 107 forms a hadron gas. This process, referred to as a chemical freeze-out, occurs at about 160 MeV [48–50]. The
 108 hadrons formed in this stage continue to interact with each other, but have energies below the threshold for
 109 inelastic particle production, resulting mainly in modifications to their momentum spectra. This continues
 110 till the medium cools further and reaches what is called a thermal freeze-out at 100–150 MeV [51–54].

111 The QGP was initially thought to be a weakly coupled parton gas because of asymptotic freedom from
 112 QCD. The highly energetic collisions such as those at the LHC would imply weak interactions between the

113 partons that make up the plasma [35, 55, 56]. This would result in rare scatterings between the constituents
 114 of the gas, washing out any spatial anisotropies based on “lumpy”-ness of the colliding nuclei or the collision
 115 geometry. On the other hand, a strong coupling within the QGP would result in the pressure gradients in
 116 the medium being driven by hydrodynamics and spatial anisotropies would be transformed to momentum
 117 anisotropies in the particles produced as shown in Figure 1.6 [57]. In this picture, the non-uniform structure
 118 of the colliding nuclei would cause a momentum anisotropy [58] that would be further enhanced when looking
 119 at collisions that are less central and do not have perfect overlap between the colliding nuclei [59, 60]. These
 120 observations were seen in azimuthal correlation measurements implying that the medium is indeed strongly
 121 coupled [61–64].

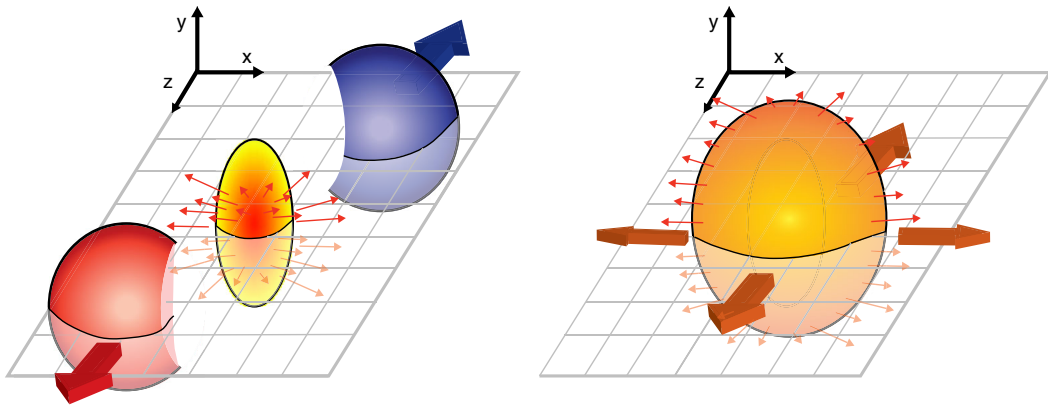


Figure 1.6: Schematic diagrams of the initial overlap region (left) and the final spatial anisotropy generated (right). Taken from [65].

122 The azimuthal angular distribution of particles produced in a heavy ion collision can be expanded in a
 123 Fourier series as [66]:

$$\frac{d\bar{N}}{d\phi} = \frac{N}{2\pi} \left(1 + 2 \sum_{n=1}^{\infty} v_n \cos(n(\phi - \Psi_n)) \right). \quad (1.5)$$

124 where N is the particle yield, ϕ is the azimuthal angle in the transverse plane and Ψ_n is the orientation of
 125 the n^{th} order symmetry plane and is called the reaction plane. The reaction plane, along with the participant
 126 plane, are shown in Figure 1.7. The coefficient $v_n = \langle \cos[n(\phi_i - \Psi_n)] \rangle$ is the magnitude of the n^{th} order
 127 azimuthal anisotropy, and is referred to as the flow harmonic. The first harmonic v_1 is called directed flow
 128 because it indicates a particular direction, while the second harmonic v_2 is called elliptic flow since the
 129 azimuthal distribution in polar coordinates for $v_2 \neq 0$ is an ellipse. These are shown in Figure 1.8 [67]. The
 130 azimuthal correlations that are a result of flow can be described by relativistic hydrodynamics [68, 69]. A

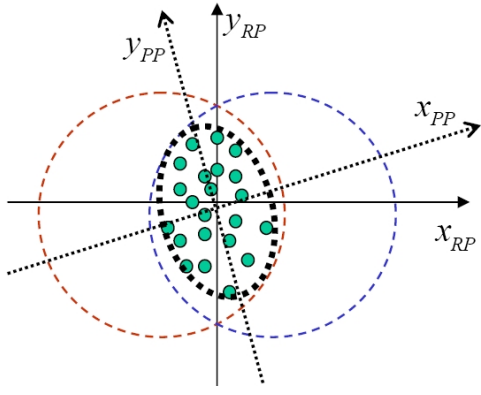


Figure 1.7: Definitions of the Reaction and Participant Plan coordinate systems. Figure taken from Ref. [67].

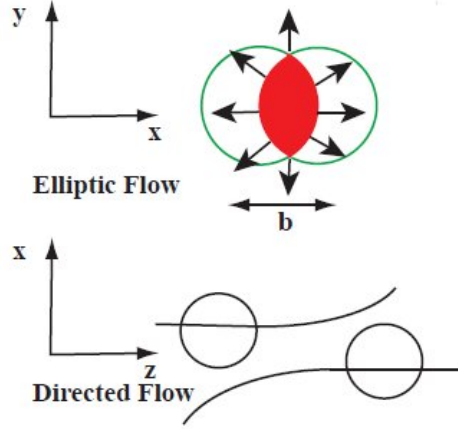


Figure 1.8: Schematics of elliptic and directed flow. Figure taken from Ref. [67].

¹³¹ comparison of anisotropies measured in terms of v_n in Ref. [70] and a hydrodynamic model described in
¹³² Ref. [71] is shown in Figure 1.9.

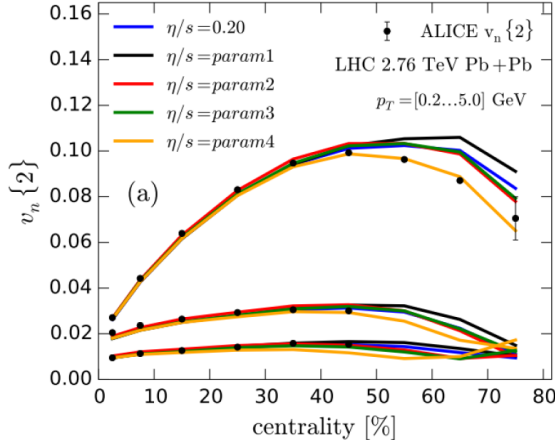


Figure 1.9: Comparison of a hydrodynamic model from [71] to anisotropy measurements by ALICE [70] for different parameterizations of η/s and for different v_n , $n = 2, 3, 4$ from top to bottom, as a function of collision centrality. Figure taken from Ref. [57].

¹³³ The measured anisotropies can be used to constrain the specific viscosity given by the ratio of viscosity
¹³⁴ to entropy density, η/s , and have shown that the QGP is a near perfect liquid with an η/s of near the
¹³⁵ theoretical minimum of $1/4\pi$ [72, 73]. In fact, this low shear viscosity is what allows the initial fluctuations
¹³⁶ in the energy density to survive the chemical freeze-out.

¹³⁷ 1.3 Heavy Ion Collisions

¹³⁸ Heavy ion collisions are a tool that can be used as a tool to study the quark-gluon plasma (QGP) [34]. In a
¹³⁹ heavy ion collision, the colliding nuclei are accelerated to relativistic energies and due to relativistic length
¹⁴⁰ contraction, form discs. In the case of a Pb+Pb collision, the relativistic γ factor is approximately 3000.
¹⁴¹ Each nucleus contains many colored quarks and antiquarks, with three more quarks than anti-quarks per
¹⁴² nucleon, with the $q\bar{q}$ popping in and out of the vacuum due to quantum fluctuations. These $q\bar{q}$ pairs are
¹⁴³ sources of transverse color fields and the corresponding force carriers, the gluons.

¹⁴⁴ When these pancake-like discs collide, their color fields interact and there is a color charge exchange,
¹⁴⁵ producing longitudinal color fields that fill the space between the receding discs. The energy densities attained
¹⁴⁶ at RHIC and the LHC are as low as $1\text{GeV}/\text{fm}^3$ [74] and $12\text{GeV}/\text{fm}^3$ [75, 76] respectively, both of which are
¹⁴⁷ above the $0.2 - 1\text{GeV}/\text{fm}^3$ energy density range required to form the QGP [77, 78].

¹⁴⁸ After the collision the energy density between the receding nuclei starts to decrease as the QGP cools and
¹⁴⁹ expands. This process, seen in Figure 1.10, continues till the energy density drops to below that within a
¹⁵⁰ hadron and the fluid “hadronizes”. These individual hadrons briefly scatter off of each other before they
¹⁵¹ freely fly towards the detector (freeze-out).

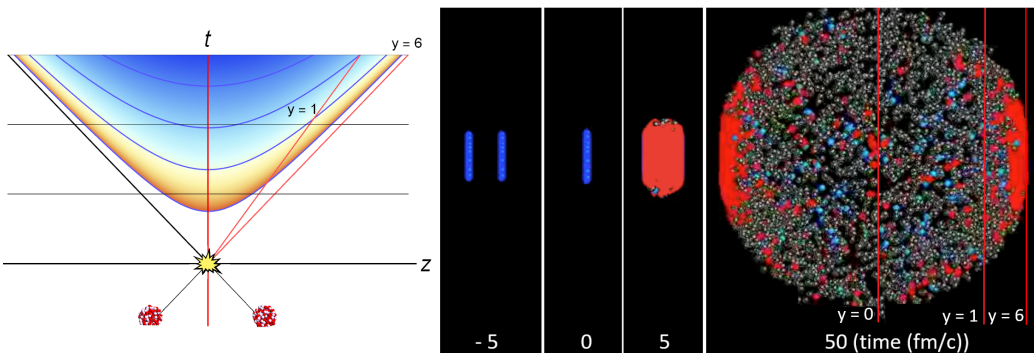


Figure 1.10: (left) Space-time diagram for a heavy ion collision. The color is indicative of the temperature of the QGP formed. (right) Snapshots of a heavy ion collision at $\sqrt{s_{\text{NN}}} = 2.76 \text{ TeV}$ at different times. The Lorentz contracted nuclei are in blue while the QGP is in red. Figure from Reference [57].

¹⁵² While Figure 1.10 shows snapshots of a head on (central) collision between two large nuclei, it is possible
¹⁵³ to have collisions where the impact parameter is larger and hence the overlap region is smaller. These
¹⁵⁴ collisions, called peripheral collisions, qualitatively undergo the same process described above, with the size
¹⁵⁵ and shape of the QGP being different. A schematic of both central and peripheral collisions is shown in
¹⁵⁶ Figure 1.11.

¹⁵⁷ The basic parameters of a heavy ion collision such as the number of participants N_{part} and number of

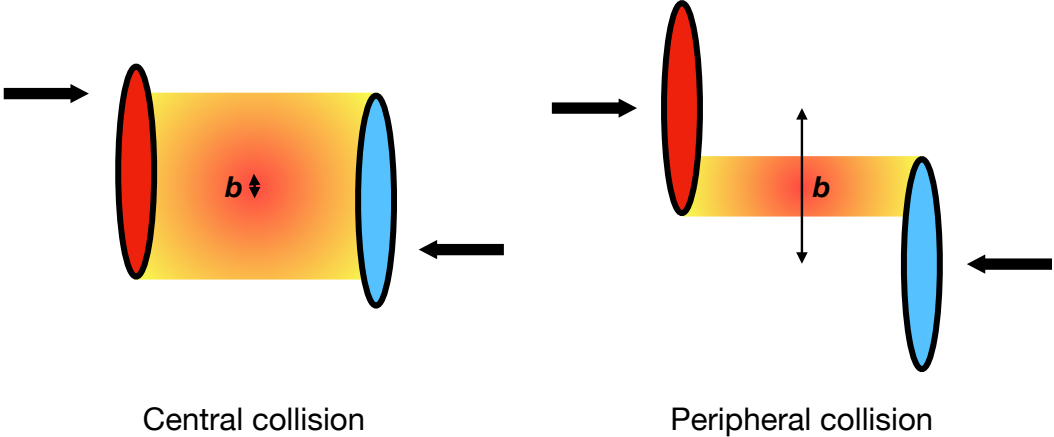


Figure 1.11: A schematic of central (left) and peripheral (right) heavy ion collisions. The impact parameter is given by b .

158 binary collisions N_{coll} can be determined using the Glauber Monte Carlo simulations [79, 80]. This technique
 159 considers a nucleus-nucleus collision as a collection of independent binary nucleon-nucleon collisions; the
 160 colliding nuclei are modeled as a set of uncorrelated nucleons being positioned within the nucleus based on a
 161 the nuclear density function uniform in azimuthal and in polar angles. The nuclear density function in this
 162 model is a parameterized Fermi distribution given by:

$$\rho(r) = \rho_0 \frac{1 + w(r/R)^2}{1 + e^{\frac{r-R}{a}}} \quad (1.6)$$

163 where ρ_0 is the nucleon density, R is the nuclear radius, a is the skin depth, w corresponds to deviations
 164 from a circular shape and is typically zero for larger nuclei like Cu, W, Au, Pb, and U. For the Pb nuclei
 165 used at the LHC, $w = 0$, $R = 6.62$ fm and $a = 0.55$ fm [81]. The nuclear density distribution for Au and Cu
 166 is shown in Figure 1.12.

167 They are then arranged with a random impact parameter b based on the distribution $d\sigma/db = 2\pi b$ and
 168 projected onto the $x - y$ plane as shown in Figure 1.13. They are then made to travel on straight trajectories,
 169 colliding if $d \leq \sqrt{\sigma_{\text{inel}}^{\text{NN}}/\pi}$, where d is the distance between the nucleons in a plane transverse to the beam
 170 axis and $\sigma_{\text{inel}}^{\text{NN}}$ is the inelastic scattering cross section. [82, 83]

171 An important parameter for colliding nuclei A and B with A and B nucleons is the thickness function
 172 T_{AB} . It describes the effective overlap area in which specific nucleons in the two colliding nuclei can interact.
 173 It can be defined in terms of the probability per unit area of a given nucleon being located at a particular
 174 distance s within the nucleus. For the colliding nuclei A and B, this is given by $T_A(\mathbf{s}) = \int \rho_A(\mathbf{s}, z_A) dz_A$ and

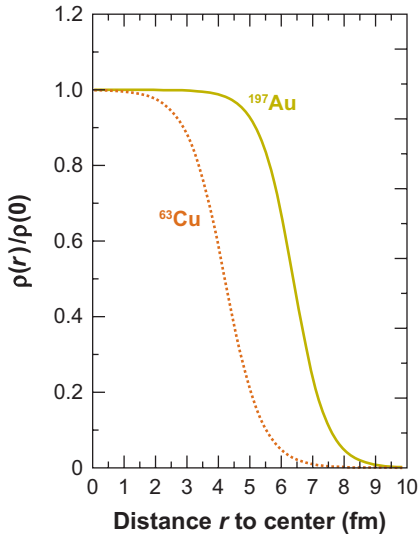


Figure 1.12: The nuclear density distributions for nuclei used at RHIC: Cu ($w = 0$, $R = 4.2$ fm and $a = 0.48$ fm) and Au ($w = 0$, $R = 6.38$ fm and $a = 0.535$ fm) [81]. Figure taken from Ref. [82].

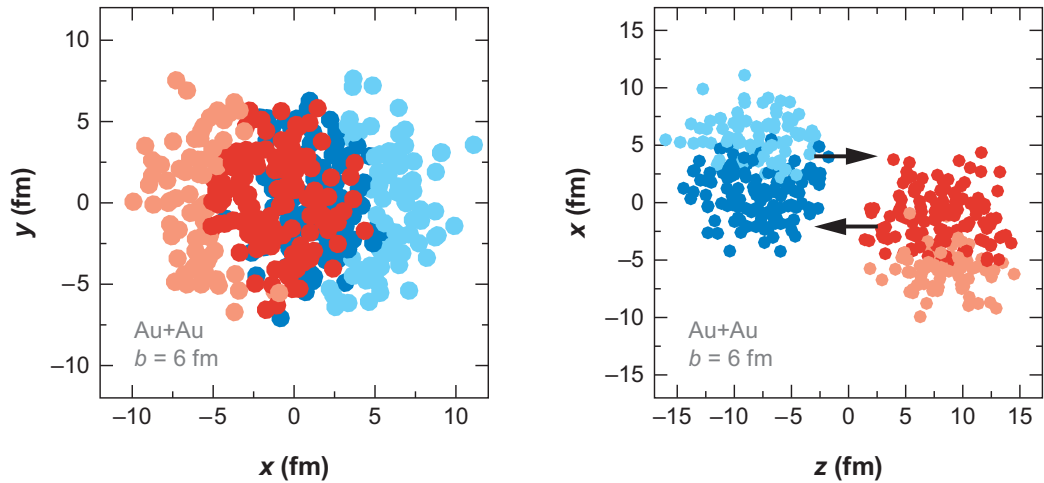


Figure 1.13: A Glauber Monte Carlo event for $Au + Au$ at $\sqrt{s_{NN}} = 200$ geV with impact parameter of 6 fm viewed in the (left) transverse plane and (right) along the beam axis. Darker circles represent the participating nucleons. Taken from [82].

¹⁷⁵ $T_B(\mathbf{s}) = \int \rho_B(\mathbf{s}, z_B) dz_B$. Then, T_{AB} is given by

$$T_{AB}(\mathbf{b}) = \int T_A(\mathbf{s}) T_B(\mathbf{s} - \mathbf{b}) d^2 s \quad (1.7)$$

¹⁷⁶ The probability of then having n interactions between nuclei A and B is given by the binomial distribution:

$$P(n, \mathbf{b}) = \binom{AB}{n} \left[T_{AB}(\mathbf{b}) \sigma_{\text{inel}}^{\text{NN}} \right]^n \left[1 - T_{AB}(\mathbf{b}) \sigma_{\text{inel}}^{\text{NN}} \right]^{AB-n} \quad (1.8)$$

¹⁷⁷ where the first term is the number of combinations for finding n collisions from AB possibilities, the second
¹⁷⁸ term is the probability for having exactly n collisions, and the last term the probability of $AB - n$ misses.
¹⁷⁹ Then the total probability of an interaction between A and B is:

$$\frac{d^2 \sigma_{\text{inel}}^{\text{AB}}}{db^2} \equiv p_{\text{inel}}^{\text{AB}}(b) = \sum_{n=1}^{AB} P(n, \mathbf{b}) = 1 - \left[1 - T_{AB}(\mathbf{b}) \sigma_{\text{inel}}^{\text{NN}} \right]^{AB} \quad (1.9)$$

¹⁸⁰ Then the total cross section is given by

$$\sigma_{\text{inel}}^{\text{AB}} = \int_0^\infty 2\pi b db \left[1 - \left(1 - T_{AB}(\mathbf{b}) \sigma_{\text{inel}}^{\text{NN}} \right)^{AB} \right] \quad (1.10)$$

¹⁸¹ and N_{coll} and N_{part} are given by [84, 85]:

$$N_{\text{coll}}(b) = \sum_{n=1}^{AB} n P(n, b) = AB \times T_{AB}(b) \sigma_{\text{inel}}^{\text{NN}} \quad (1.11)$$

$$N_{\text{part}}(b) = A \int T_A(\mathbf{s}) \left[1 - \left(1 - T_B(\mathbf{s} - \mathbf{b}) \sigma_{\text{inel}}^{\text{NN}} \right)^B \right] d^2 s + B \int T_B(\mathbf{s} - \mathbf{b}) \left[1 - \left(1 - T_A(\mathbf{s}) \sigma_{\text{inel}}^{\text{NN}} \right)^A \right] d^2 s \quad (1.12)$$

¹⁸² The correlation between N_{coll} and N_{part} can be seen in Figure 1.14:

¹⁸³ The charged particle multiplicity N_{ch} along with the combination of N_{part} and impact parameter b can
¹⁸⁴ be used to determine the centrality of a heavy ion event. An example of this is shown in Figure 1.15.

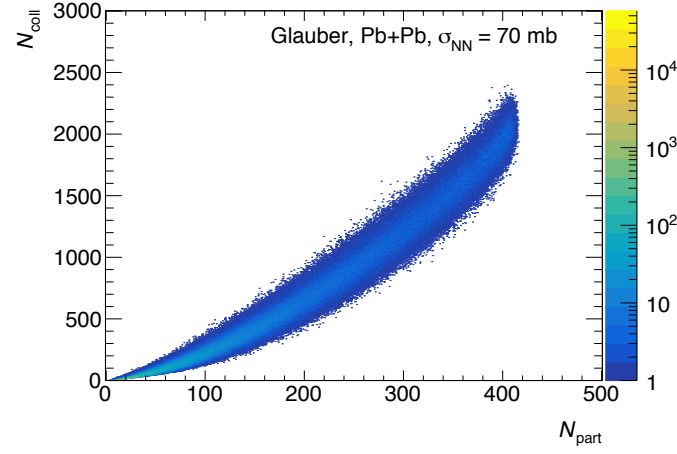


Figure 1.14: The $N_{\text{coll}} - N_{\text{part}}$ correlation for Pb+Pb collisions at $\sqrt{s_{\text{NN}}} = 5.02 \text{ TeV}$. Taken from [86].

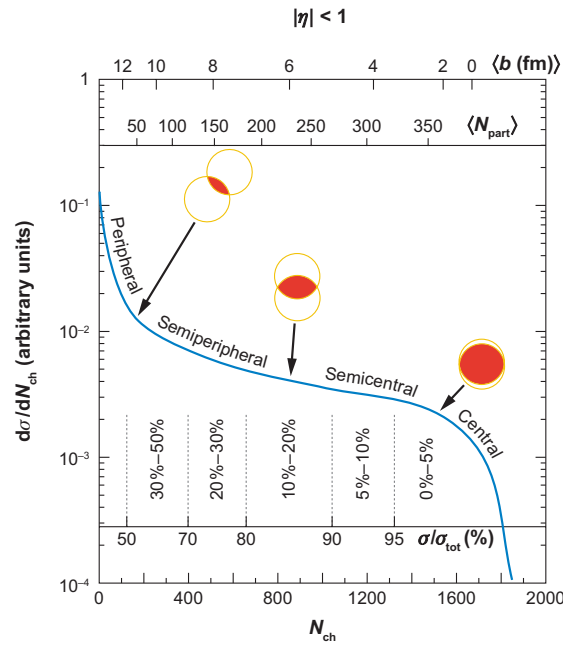


Figure 1.15: The correlation between the observable N_{ch} and N_{part} to determine the centrality distribution. Taken from [82].

185 1.4 Jets and Jet Quenching

186 As colored objects start to fly apart in a particle collision, the energy required to separate them increases
 187 as a natural consequence of color confinement. If the energy with which they are flying apart is greater
 188 than the energy required to separate them, it becomes more favorable to produce a quark-antiquark ($q\bar{q}$)
 189 pair between the original two quarks. This process of $q\bar{q}$ production continues recursively until it is not
 190 energetically favorable to do so, with the end result being conical sprays of hadrons called jets. This picture
 191 is qualitatively supported by Lattice QCD [87]. A schematic of this process is shown in Figure 1.16. Because
 192 of their color charge, gluon led jets have a softer fragmentation and result in more particles carrying lesser
 193 energy as compared to quark led jets [88].

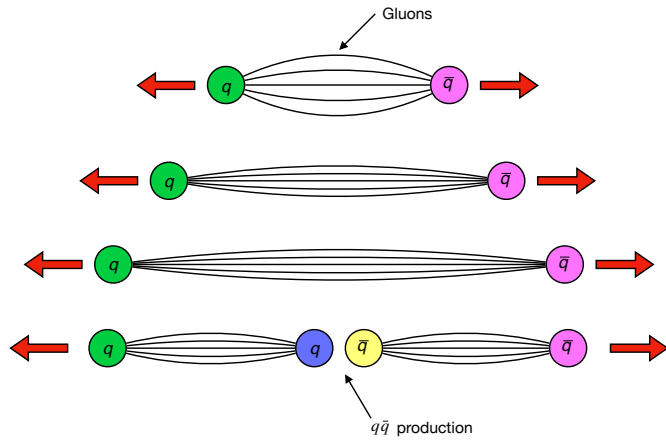


Figure 1.16: A schematic of how jets are produced from a hard process involving $q\bar{q}$. The “gluonic flux tubes” build up and break as the quarks gain energy, and result in the formation of new $q\bar{q}$ pairs.

194 1.4.1 Jets in e^+e^- collisions

195 The simplest process that can be used to study jets is the process $e^+e^- \rightarrow q\bar{q} \rightarrow 2$ jets. The electron and
 196 positron annihilates to produce a photon that can decay into a $q\bar{q}$ pair, that hadronize and form jets. In
 197 fact, this was the process that provided experiment evidence of jets at SPEAR (Stanford Positron Electron
 198 Accelerating Ring) at SLAC in 1975, where it was observed that the distribution of final state hadrons
 199 was not isotropic [89, 90] Analyses of these distributions showed that they were associated with spin 1/2
 200 quarks. Jets in e^+e^- collisions further provided the first indirect evidence of gluons when three jet events
 201 were observed in the $\Upsilon \rightarrow ggg$ decay [91, 92]. At the Large Electron-Positron Collider (LEP), higher collision
 202 energies allowed the $e^+e^- \rightarrow Z^0 \rightarrow q\bar{q}$ process. In these processes, to leading order, the $q\bar{q}$ pair evolved via
 203 gluon radiation before converting to hadrons [93], allowing for events with more than two jets. Jet production

204 in e^+e^- collisions is also one of the best ways to test the validity of perturbative QCD [94].

205 1.4.2 Jets in pp collisions

206 Jet production in a vacuum is well described in context of perturbative QCD [95]. Processes involving large
 207 momentum transfers like high p_T hadron production as shown in Figure 1.17.

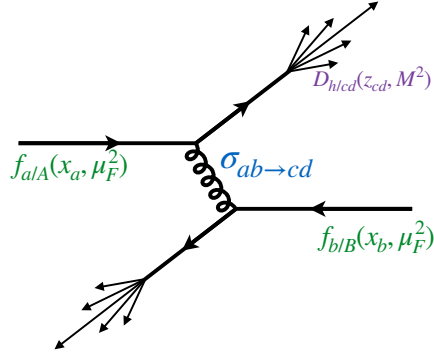


Figure 1.17: Jet production from the process $pp \rightarrow hX$, factorizing in terms of the parton distribution functions, scattering cross sections, and jet fragmentation functions [96].

208 These processes can be described in terms of the parton distribution functions, scattering cross sections,
 209 and final state fragmentation functions as shown below [96]:

$$d\sigma_{pp \rightarrow hX} \approx \sum_{abjd} \int dx_a \int dx_b \int dz_j f_{a/p}(x_a, \mu_f) \otimes f_{b/p}(x_b, \mu_f) \otimes d\sigma_{ab \rightarrow jd}(\mu_f, \mu_F, \mu_R) \otimes D_{j \rightarrow h}(z_j, \mu_f) \quad (1.13)$$

210 where $x_a = p_a/P_A, x_b = p_b/P_b$ are the initial momentum fractions carried by the interacting partons,
 211 $z_j = p_h/p_j$ is the momentum fraction carried by the final observed hadron. $f_{a/p}(x_a, \mu_f)$ and $f_{b/p}(x_b, \mu_f)$ are
 212 the two parton distribution functions (PDFs), $d\sigma_{ab \rightarrow jd}(\mu_f, \mu_F, \mu_R)$ is the differential cross section for parton
 213 scattering and $D_{j \rightarrow h}(z_j, \mu_f)$ is the fragmentation function (FFs) for parton j to hadron h . μ_f and μ_F are the
 214 factorization scales and μ_R is the renormalization scale, and are typically taken to be the same hard scale Q .
 215 The PDFs characterize the initial state and represent the probability of finding a parton with longitudinal
 216 momentum fraction x (shown in Figure 1.18) in the initial hadron, while the FFs describe the probability of
 217 fragmenting to a hadron h with given kinematic properties.

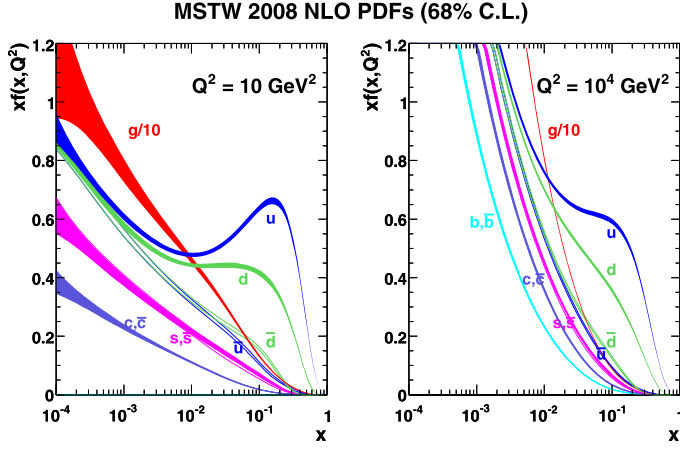


Figure 1.18: The next to leading order (NLO) PDFs at (left) $Q^2 = 10 \text{ GeV}^2$ and (right) $Q^2 = 10^4 \text{ GeV}^2$. The band is the associated one-sigma (68%) confidence level uncertainty. Taken from [97].

218 Jet cross sections in pp and $\partial\bar{p}$ collisions measured by a variety of different experiments are shown in
219 Figure 1.19.

220 1.4.3 Jets in heavy ion collisions

221 In the case of heavy ion collisions, the jet observables can be modified due to two sources: the nuclear PDF
222 being distinct from a proton PDF, and the formation of the quark gluon plasma.
223 The former is collectively referred to as cold nuclear matter (CNM) effect, and can be quantified by
224 defining a nuclear modification factor for the PDF:

$$R_a^A(x, Q^2) = \frac{f_{a/A}(x, Q^2)}{f_{a/p}(x, Q^2)} \quad (1.14)$$

225 where $f_{a/A}$ and $f_{a/p}$ are the nuclear and proton PDFs respectively. This R_a^A factor is determined by global
226 fits to data from DIS measurements [99–101]. CNM effects include the following contributions:

- 227 • Shadowing: This is a destructive interference effect that reduces the interactions of a nucleon incident
228 on a nucleus within its interior and on its back face. This effect reduces the effective number of nucleons
229 in an inelastic interaction to $A^{2/3}$. For Q^2 of the order of a few GeV^2 , this effect dominates for $x < 0.05$
230 and implies $R_a^A(x, Q^2) < 1$ [102].
- 231 • Anti-shadowing: This compensates for the shadowing effect based on the momentum sum rule, and for
232 Q^2 of the order of a few GeV^2 implies $R_a^A(x, Q^2) > 1$ over the region $0.05 < x < 0.20$.

Jet Production in pp and $\bar{p}p$ Interactions

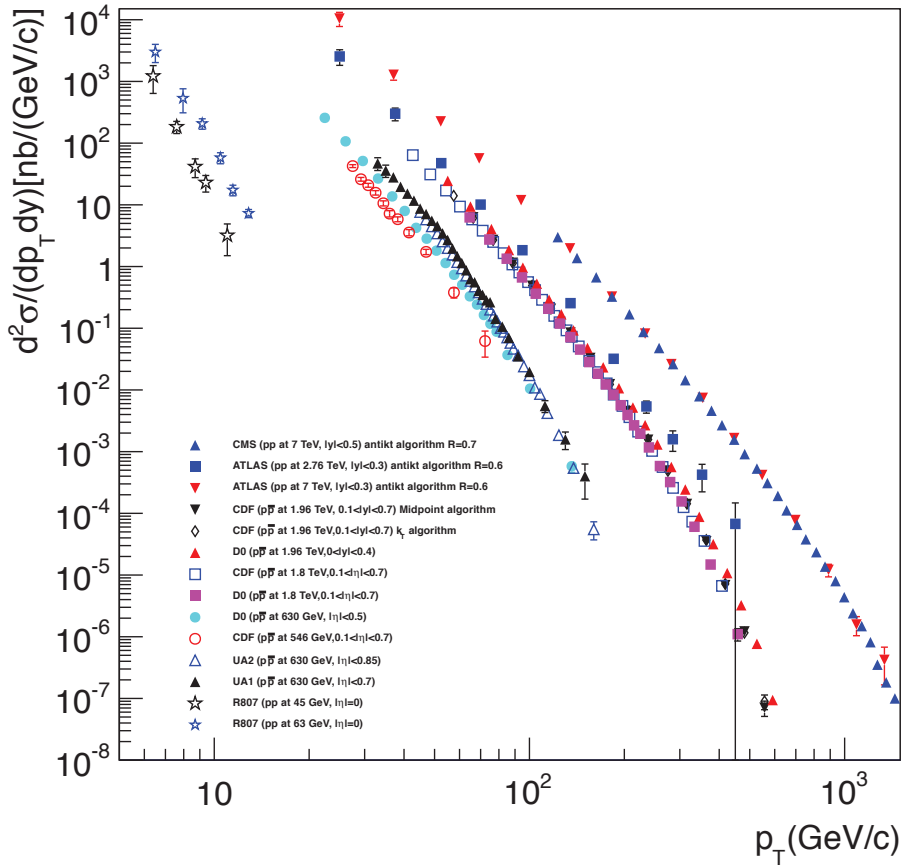


Figure 1.19: Inclusive differential jet cross sections shown as a function of jet transverse momentum from different experiments. Figure taken from [98].

233 • EMC: The modification of the nuclear structure function was first observed by the European Muon
 234 Collaboration [103]. Recent observations have suggested that the effect is caused by short-range
 235 correlated nucleon pairs within nuclei [104]. For Q^2 of the order of a few GeV^2 , this effect dominates
 236 for $0.2 < x < 0.80$ and implies $R_a^A(x, Q^2) < 1$.

237 • Fermi Motion: This effect considers the motion of the nucleons within the nucleus. It results in
 238 $R_a^A(x, Q^2) > 1$ over the $x > 0.8$ region for Q^2 of the order of a few GeV^2 [105].

239 Cold nuclear matter effects are experimentally measured using $p + A$ systems where the size and shape of
 240 the plasma, and hence any effects thereof, are a lot smaller.

241 The second source of modification is the formation of the hot and dense quark gluon plasma. The hot
 242 nuclear matter effects further serve as an independent confirmation that the medium formed is strongly
 243 interacting. Jets are formed early enough that they traverse the Quark Gluon Plasma and as strongly
 244 interacting particles, are both affected by, and affect the QGP. This interaction typically results in the jet
 245 losing energy and forward momentum [106, 107], with the lost energy being deposited in the medium [108].
 246 Jets can also pick up momentum transverse to the parton direction [109]. The hot nuclear matter effects can
 247 be considered to be a combination of collisional and radiative energy losses summarized in Figure 1.20.

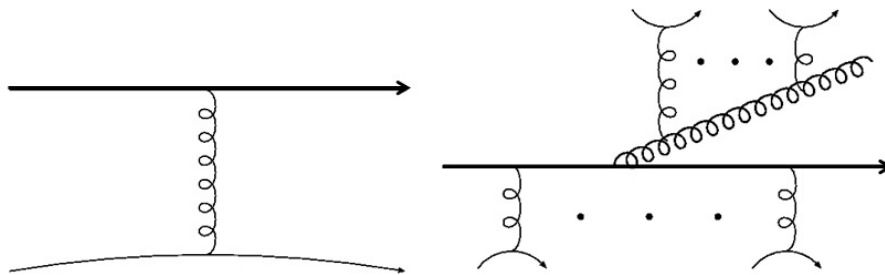


Figure 1.20: The typical diagrams for (left) collisional and (right) radiative energy losses for a parton in a hard scattering as it propagates through the QGP. Taken from [96]

- 248 • Collisional energy loss: This is a combination of elastic and inelastic collisions of the hard parton with
 249 the constituents of the quark gluon plasma.
- 250 • Radiative energy loss: This is the larger source of parton energy loss and jet quenching. These are
 251 modified by the presence of the plasma due to scatterings off of the plasma constituents. A variety of
 252 radiative energy loss frameworks that have been developed include: Baier-Dokshitzer-Mueller-Peigne-
 253 Schiff-Zakharov (BDMPS-Z) [110], Gyulassy, Levai and Vitev (GLV) [111], Amesto-Salgado-Wiedemann
 254 (ASW) [112], Arnold-Moore-Yaffe (AMY) [113] and higher twist (HT) [114].

Both hot and cold nuclear matter effects can be described by modifying Equation 1.13 as:

$$\begin{aligned} d\sigma_{AB \rightarrow hX} &\approx \sum_{abjj'd} f_{a/A}(x_a) \otimes f_{b/B}(x_b) \\ &\otimes d\sigma_{ab \rightarrow jd}(\mu_f, \mu_F, \mu_R) \\ &\otimes P_{j \rightarrow j'} \\ &\otimes D_{h \rightarrow j'}(z_j, \mu_f) \end{aligned} \quad (1.15)$$

where the additional $P_{j \rightarrow j'}$ describes the interaction of the hard parton with the colored medium. This is typically taken as part of the fragmentation modification as:

$$\tilde{D}_{h \rightarrow j'}(z_j, \mu_f) \approx \sum_{j'} P_{j \rightarrow j'}(p_{j'} | p_j) \otimes D_{h \rightarrow j'}(j') \quad (1.16)$$

1.4.4 Jet Reconstruction

Jets can be reconstructed by clustering algorithms that take in a variety of inputs. The algorithm used in ATLAS is the anti- k_t clustering algorithm [115]. This algorithm clusters soft particles around hard ones in the following manner:

- Calculate all distances d_{ij} between entities i and j , and distance d_{iB} between entity i and beam B .
- Identify the smallest distances such that for the smallest distance d_{ij} , the entities i and j are combined and return to beginning.
- If the smallest distance is d_{iB} , then take i as the jet and remove it from the list of entities and return to beginning.
- Continue the procedure till the list of items is empty.

In general the distance d_{ij} between the objects is found via the prescription

$$d_{ij} = \min(k_{Ti}^{2p}, k_{Tj}^{2p}) \frac{\Delta_{ij}^2}{R^2} \quad (1.17)$$

$$d_{iB} = k_{Ti}^{2p} \quad (1.18)$$

268 where k_{Ti} is the transverse momentum of particle i and $\Delta_{ij} = \sqrt{\Delta\eta_{ij}^2 + \Delta\phi_{ij}^2}$ is the distance between
 269 particles i and j in $\eta - \phi$ space. R the distance parameter and reflects the size of the jet being considered. In the
 270 case of the anti- k_t algorithm, $p = -1$. Other popular clustering algorithms like k_t [116] and Cambridge/Aachen
 271 [117] use $p = 1$ and $p = 0$ respectively. The behavior of the different clustering algorithms is shown in
 272 Figure 1.21.

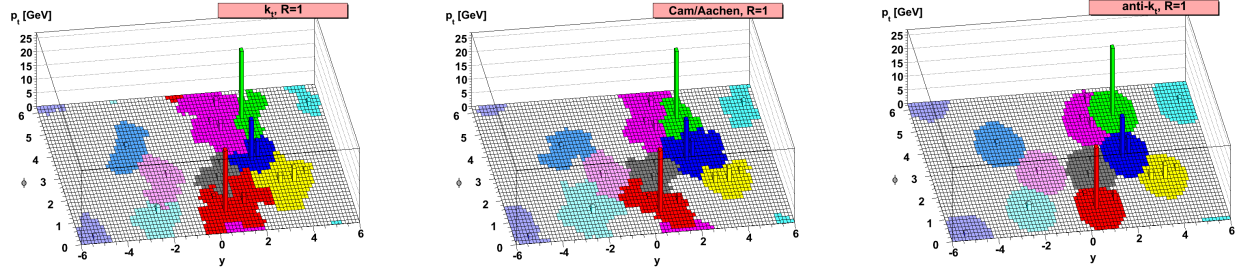


Figure 1.21: Different clustering algorithms applied to the sample parton-level event. Figure taken from [115].

273 The popularity of the anti- k_t algorithm comes from its overcoming of two common problems: collinear
 274 and infrared safety. These are related to instabilities in the cones that are found due to soft radiation.

275 Figure 1.22 describes the collinear safety problem. In a collinear safe jet algorithm, the presence of a virtual
 276 loop or a collinear splitting of a central particle would not change the number of jets being reconstructed.
 277 On the other hand, while a collinear unsafe jet algorithm would not change its output with the presence
 278 of a virtual loop, a splitting in the central particle would lead to the left and right most particles forming
 279 individual seeds, implying two reconstructed jets [118].

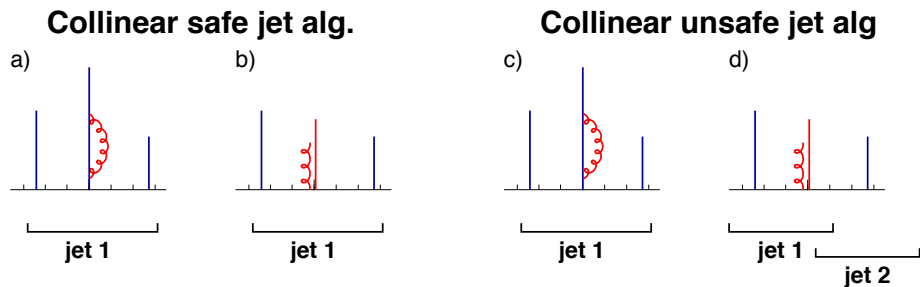


Figure 1.22: An illustration of collinear unsafe behavior. The particle p_T is proportional to the height and the horizontal axis indicates rapidity. Taken from [118].

280 A schematic describing infrared safety problem is shown in Figure 1.23. Here an infrared safe algorithm
 281 would use the three particles as seeds iteratively find two stable cones. An unsafe algorithm however would
 282 find three overlapping cones based on the addition of a soft seed.

283 For heavy ion collisions in ATLAS, the inputs to the algorithm are the $\eta \times \phi = 0.1 \times 0.1$ calorimeter

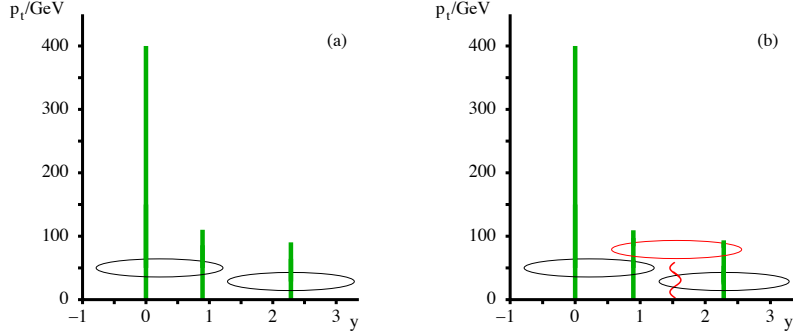


Figure 1.23: An illustration of infrared unsafe behavior. The particle p_T is proportional to the height and the horizontal axis indicates rapidity. Taken from [119].

towers. The tower energies are determined by summing up the energies of the individual calorimeter cells.
 The anti- k_t algorithm is first run with the distance parameter $R = 0.2$, following which an underlying event subtraction procedure is performed. A first estimate of the average underlying event energy density $\rho_i(\eta)$ is done in 0.1 slices of η in each calorimeter layer i after excluding the regions that overlap with the seed jets.
 A modulation of $2v_2 \cos[2(\phi - \Psi_2)]$ is applied to account for the flow from the QGP and the underlying event is subtracted to give E_{Tj}^{sub} :

$$E_{Tj}^{\text{sub}} = E_{Tj} - A_j \rho_i(\eta_j) \left(1 + 2 \sum_{n=2}^4 v_{ni} (\cos[2(\phi - \Psi_n)]) \right) \quad (1.19)$$

where E_{Tj} , η_j , ϕ_j and A_j are the cell E_T , η , ϕ and area for cell j in layer i . This process is done iteratively done one more time after getting new seeds with the distance parameter $R = 0.2$ and excluding areas that are within $\Delta R = 0.4$ of the seeds. Updated values of ρ'_i and v'_2 are recalculated and used to estimate the background that is subtracted from the original cell energies. More details on this procedure can be found in [120].

Chapter 2

Major Jet Measurements

295 This chapter shall discuss some important experimental jet measurements that motivate the study of the
296 main analysis in this thesis. These include the study of the jet yields, dijet asymmetry, and jet fragmentation.
297 It shall then go on to discuss a few models that have been used to explain the data, looking in particular at
298 the following: Effective Quenching (EQ), Soft Collinear Effective Theory (SCET), Hybrid Model, and Jet
299 Fluid Model.

300 2.1 Dijet Balance: x_J

301 This section will discuss the dijet balance for $R = 0.4$ jets as measured by ATLAS detector for Pb+Pb
302 collisions at $\sqrt{s_{\text{NN}}} = 2.76$ TeV [121]. The dijet imbalance can be expressed in terms of x_J defined as

$$x_J = \frac{p_{\text{T}2}}{p_{\text{T}1}} \quad (2.1)$$

303 where $p_{\text{T}2}$ and $p_{\text{T}1}$ are the transverse momenta of the two highest- p_{T} jets in the event respectively. The
304 minimum $p_{\text{T}2}$ considered is 25 GeV and the pair of jets are separated by $|\Delta\phi| > 7\pi/8$. The dijet yields
305 normalized by the number of jets and determined as $1/N_{\text{jets}} dN/dx_J$ are presented as a function of x_J for
306 different centrality intervals, as well as different ranges for $p_{\text{T}1}$. The measured distributions are further
307 unfolded to remove detector resolution effects and allow comparison to theoretical models.

308 Figure 2.1 shows the x_J distribution for dijet pairs in pp and Pb+Pb collisions in two different centrality
309 bins and two $p_{\text{T}1}$ ranges. It can be seen that the dijet yields in pp are peaked at unity and become narrower
310 for larger $p_{\text{T}1}$ ranges. This reflects the fact that the effects of jet quenching are minimal and the higher- p_{T}
311 jets are better balanced. The dijet yields in peripheral Pb+Pb collisions are similar to the distributions from
312 the pp data, showing that the effects of quenching are smaller. On the other hand, dijet yields in central
313 Pb+Pb collisions are significantly broadened, reflecting the maximal of jet quenching. This is consistent with
314 the picture of the individual jets in the dijet pair traversing different lengths in the QGP and hence losing

315 different amounts of energy. In fact, the distribution for Pb+Pb data is peaked at $x_J = 0.5$, implying a loss
 316 of 50% of the jet p_T .

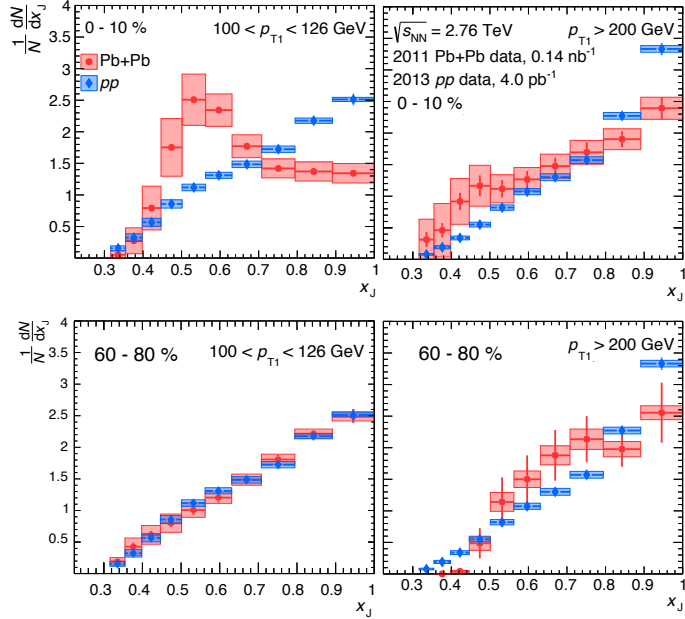


Figure 2.1: The $1/N_{\text{jets}} dN/dx_J$ distributions for $R = 0.4$ jets as a function of x_J for pp (blue) and Pb+Pb (red) collisions. The different panels are for (top) central and (bottom) peripheral collisions in (left) $100 < p_{T1} < 126 \text{ GeV}$ and (right) $p_{T1} > 200 \text{ GeV}$. The pp data is the same in all panels. The statistical uncertainties are indicated by the bars while the boxes indicate the systematic uncertainties. Figures taken from [121].

317 Further measurements of $R = 0.3$ jets are shown in Figure 2.2. These distributions are significantly flatter
 318 than the ones for $R = 0.4$ jets, an observation that is consistent with the expectation that the transverse
 319 momenta correlation between the dijet pair is weaker for jets with smaller radii due to radiation that is
 320 outside the nominal jet cone.

321 2.2 Modification of jet yields: R_{AA}

322 This section discusses the measurement of the inclusive jet R_{AA} as measured by the ATLAS detector for
 323 $R = 0.4$ jets in $\sqrt{s_{\text{NN}}} = 5.02 \text{ TeV}$ Pb+Pb collisions [122].

324 While a measurement that compares the jets in a dijet system to each other as discussed in Section 2.1
 325 can provide valuable information about how jets lose energy, it has the following limitation: If both jets lose
 326 equal amounts of energy, the dijet yield will still be peaked at unity and no new information will be obtained.
 327 Thus, it is useful to compare the jet yields directly between the pp and Pb+Pb systems and construct the jet
 328 R_{AA} observable. This is defined as:

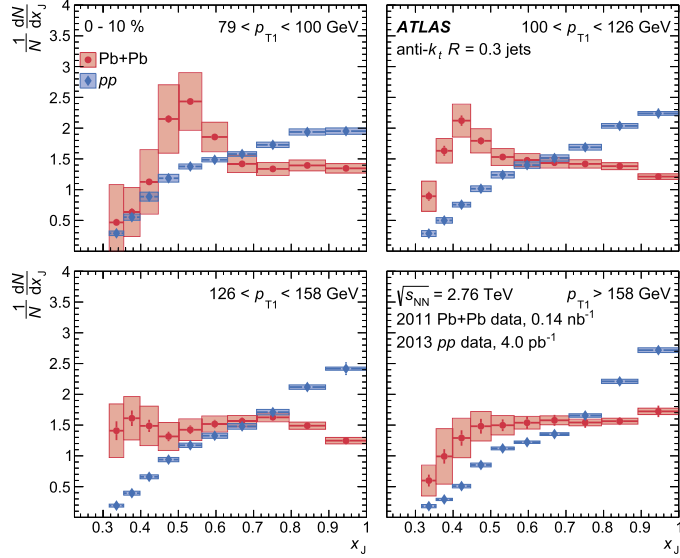


Figure 2.2: The $1/N_{\text{jets}} dN/dx_J$ distributions for $R = 0.3$ jets as a function of x_J in pp and central $\text{Pb}+\text{Pb}$ collisions. The different panels are for different, p_{T1} ranges (top left to bottom right) central and (bottom) peripheral collisions. The $\text{Pb}+\text{Pb}$ data is in red circles while the pp data is in blue diamonds and is the same in all panels. The statistical uncertainties are indicated by the bars while the boxes indicate the systematic uncertainties. Figures taken from [121].

$$R_{\text{AA}} = \frac{\frac{1}{N_{\text{evt}}} \left. \frac{d^2 N_{\text{jet}}}{dp_{\text{T}} dy} \right|_{\text{cent}}}{\langle T_{\text{AA}} \rangle \left. \frac{d^2 \sigma_{\text{jet}}}{dp_{\text{T}} dy} \right|_{\text{pp}}} \quad (2.2)$$

where T_{AA} is the nuclear thickness function and accounts for the geometric enhancement between pp and $\text{Pb}+\text{Pb}$ as discussed in Section 1.3 and [82].

This measurement was conducted for jets in the 40–1000 GeV range in different rapidity and centrality intervals. The jet yields in pp and $\text{Pb}+\text{Pb}$ collisions are shown in Figure 2.3. The $\text{Pb}+\text{Pb}$ jet yields are scaled by the thickness function and are shown for 8 centrality intervals.

Figure 2.4 shows the measured inclusive jet R_{AA} as a function of jet p_{T} for different centrality bins and jet rapidity $|y| < 2.8$. It can be seen that the most central collisions show a clear suppression with an $R_{\text{AA}} \approx 0.45$ at jet $p_{\text{T}} = 100$ GeV. The R_{AA} value slowly evolves with jet p_{T} and rises to 0.6 at jet $p_{\text{T}} = 800$ GeV. This modification becomes smaller for more peripheral collisions.

The smooth centrality dependence can be more clearly seen in Figure 2.11(a), where R_{AA} is shown as a function of $\langle N_{\text{part}} \rangle$ for jets in the 100–126 GeV and 200–251 GeV ranges. The magnitude of the suppression is also seen to significantly depend on jet p_{T} for $\langle N_{\text{part}} \rangle \geq 50$.

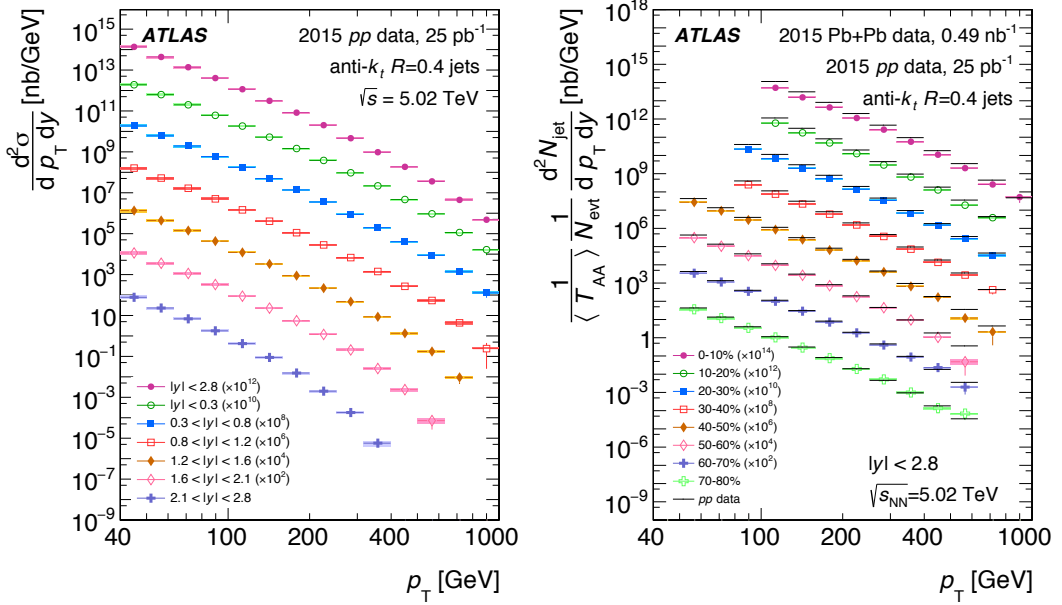


Figure 2.3: (Left) The inclusive jet cross section in pp collisions as a function of jet p_T in different $|y|$ intervals scaled by successive powers of 10^2 for visibility. (Right) Per event inclusive jet yield in $Pb+Pb$ collisions normalized by $\langle T_{AA} \rangle$ as a function of jet p_T in different centrality intervals scaled by successive powers of 10^2 for visibility. The solid lines represent the cross section from pp data at the same rapidity interval scaled by the same 10^2 factor. Figure taken from [122].

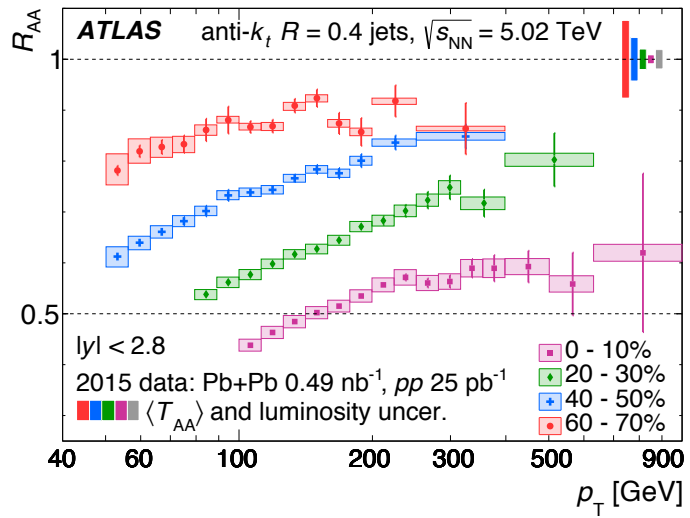


Figure 2.4: The R_{AA} distributions as a function of jet p_T for different centrality bins and jet rapidity $|y| < 2.8$. The error bars represent statistical uncertainties while the shaded boxes represent systematic uncertainties. Figure taken from [122].

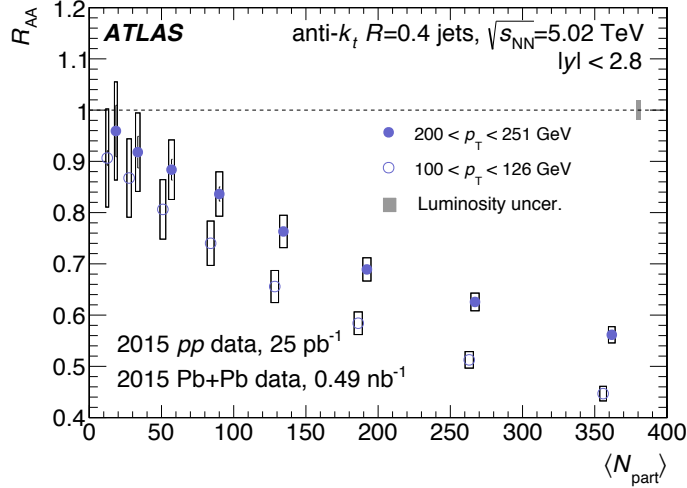


Figure 2.5: The R_{AA} distributions as a function of jet p_T for different centrality bins and jet rapidity $|y| < 2.8$. The error bars represent statistical uncertainties while the shaded boxes represent systematic uncertainties. Figure taken from [122].

2.3 Jet Fragmentation

This discussion is based on the measurement described in [123]. While measurements like R_{AA} and asymmetry describe how much energy is lost by the jet, fragmentation measurements describe the momentum distribution of particles associated to the jet. These can be described as:

$$D(z) = \frac{1}{N_{\text{jet}}} \frac{dn_{\text{ch}}}{dz} \quad (2.3)$$

$$D(p_T) = \frac{1}{N_{\text{jet}}} \frac{dn_{\text{ch}}}{dp_T} \quad (2.4)$$

where $z = p_T \cos(\Delta R / p_T^{\text{jet}})$ and gives the charged-particle longitudinal momentum fraction relative to the jet.

Modifications to the fragmentation functions in Pb+Pb collisions can be evaluated by constructing the ratios:

$$R_{D(z)} = \frac{D(z)_{\text{Pb+Pb}}}{D(z)_{\text{pp}}} \quad (2.5)$$

$$R_{D(p_T)} = \frac{D(p_T)_{\text{Pb+Pb}}}{D(p_T)_{\text{pp}}} \quad (2.6)$$

This measurement is corrected for detector effects and unfolded to the particle level. This allows for comparisons to other measurements and theoretical models. The $D(z)$ and $D(p_T)$ distributions are shown in

349 Figure ?? and Figure 2.6

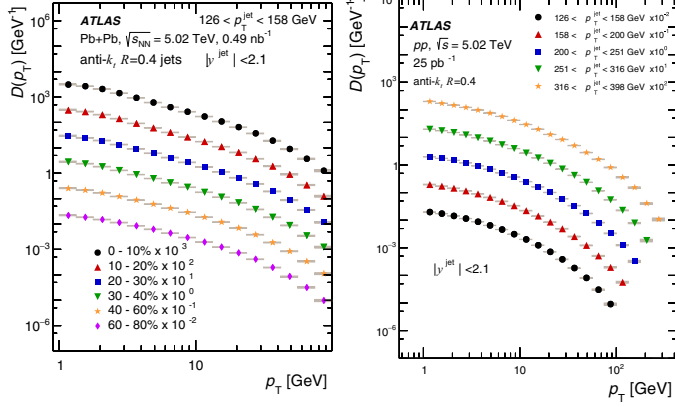


Figure 2.6: (Left) The $D(p_T)$ distributions in pp as a function of charged-particle p_T for different p_T^{jet} selections and for jet rapidity $|y| < 2.1$. (Right) The $D(p_T)$ distributions in $Pb+Pb$ as a function of charged-particle p_T for different centrality selections and for jet rapidity $|y| < 2.1$. The error bars represent statistical uncertainties while the shaded boxes represent systematic uncertainties. Figure taken from [123].

350 The modifications to the $D(z)$ distributions are shown in Figure 2.7. It can be seen that there is an excess
 351 of particles with low z and high z . These are particles that carry either a small or a large fraction of energy
 352 of the jet p_T . There is an associated depletion for particles with intermediate z . These modifications become
 353 smaller for more peripheral collisions. The p_T^{jet} dependence of the $R_{D(z)}$ and $R_{D(p_T)}$ distributions can be
 354 seen in Figure 2.8. This dependence can give insight into the modification of the fragmentation functions,
 355 with any scaling with z indicating a change in the fragmentation pattern, while a scaling with p_T reflecting an
 356 effect from the medium itself. The low momentum excess in the $R_{D(p_T)}$ distributions seen in Figure 2.8 can
 357 be further studied by integrating over that region. Then the extra number of particles in $Pb+Pb$ compared
 358 to pp is given by:

$$N_{\text{ch}} = \int_{p_{T_{\min}}}^{p_{T_{\max}}} \left(D(p_T)_{\text{Pb+Pb}} - D(p_T)_{pp} \right) dp_T \quad (2.7)$$

359 where $p_{T_{\min}} = 1 \text{ GeV}$ and $p_{T_{\max}} = 4.2 \text{ GeV}$. The N_{ch} distributions can be seen in Figure 2.9. It can be
 360 clearly seen that the size of the excess increases as a function of p_T^{jet} , growing from about 1.5 to 2.5 extra
 361 particles in the most central $Pb+Pb$ collisions. This excess is even seen in the peripheral $Pb+Pb$ collisions,
 362 though it is a lot smaller and ranges from 0.2 to 0.5 extra particles.

363 The modifications to the $D(z)$ distributions have also been compared to a variety of models, including
 364 the Effective Quenching model [124], the Soft Collinear Effective Theory [125, 126], and the Hybrid Model

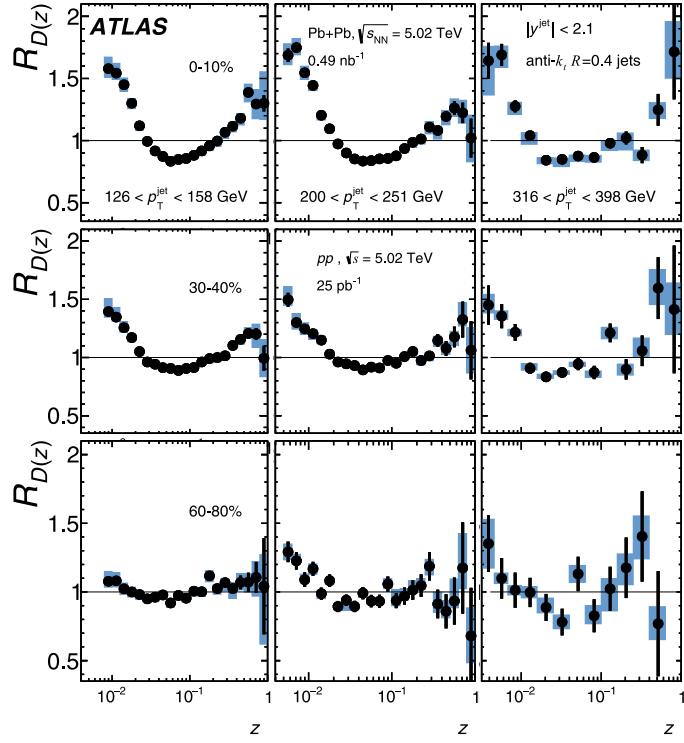


Figure 2.7: The modifications to the $D(z)$ distributions in $\text{Pb}+\text{Pb}$ compared to pp as a function of charged-particle z for different p_T^{jet} selections (left to right) and different centrality selections (top to bottom) for jet rapidity $|y| < 0.3$. The error bars represent statistical uncertainties while the shaded boxes represent systematic uncertainties. Figure taken from [123].

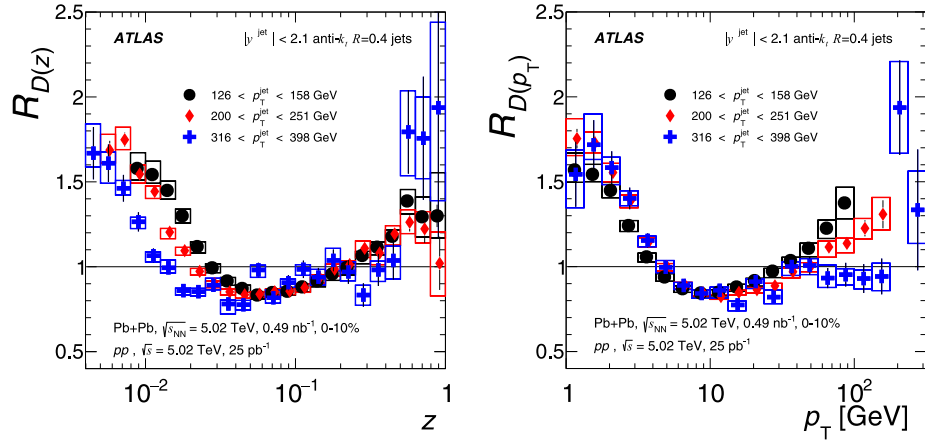


Figure 2.8: The p_T^{jet} dependence of the $R_{D(z)}$ (left) and $R_{D(p_T)}$ (right) distributions in 0–10% central $\text{Pb}+\text{Pb}$ compared to pp collisions. The error bars represent statistical uncertainties while the shaded boxes represent systematic uncertainties. Figure taken from [123].

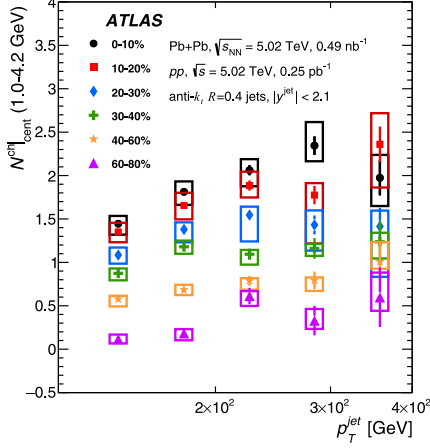


Figure 2.9: The number of extra particles that carry $1 < p_T < 4$ GeV in $\text{Pb}+\text{Pb}$ compared to pp . The different colors represent different centrality selections. The error bars represent statistical uncertainties while the shaded boxes represent systematic uncertainties. Figure taken from [123].

365 [127]. These comparisons are shown in Figure 2.10. It can be seen that

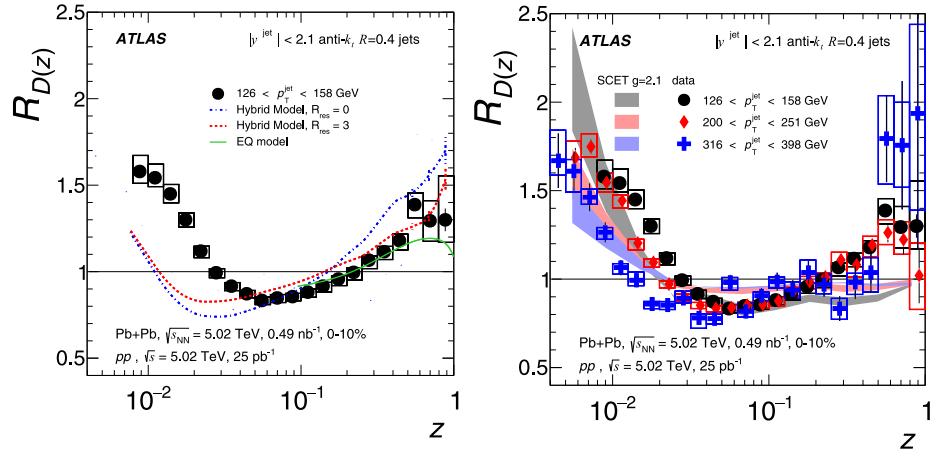


Figure 2.10: The $R_{D(z)}$ distributions compared to the EQ and Hybrid models (left) and SCET (right). The error bars represent statistical uncertainties while the shaded boxes represent systematic uncertainties. Figure taken from [123].

366 2.4 Effective Quenching

367 This discussion is based on the model introduced in Ref. [124]. This phenomenological model emphasizes
 368 the jet p_T dependence of the quark to gluon fraction and the difference between quark-jet and gluon-jet
 369 quenching. It uses an “extended” power law parameterization of the high- p_T hadron spectra coupled with a

370 quenching that is based on a non-constant fractional energy loss. This model considers the different color
371 charges carried by quarks and gluons and their different splitting functions, and assumes that gluon jets lose
372 energy at a rate 9/4 times higher than quark jets. The key assumption of the model are:

- 373 • The energy lost by a jet is radiated at large angles and does not appear within the jet cone. This is
374 backed by [128].
- 375 • The fragmentation pattern of the jet is unaffected by the presence of the QGP i.e. they fragment as
376 they would in a vacuum. This is motivated by the idea that the QGP is unable to resolve the internal
377 jet structure and is supported by [129, 130].

378 The model uses the following extended power-law parameterization to describe the high- p_T jet spectra:

$$\frac{dn}{dp_T^{\text{jet}}} = A \left(\frac{p_{T0}}{p_T^{\text{jet}}} \right)^{n+\beta \log(p_T^{\text{jet}}/p_{T0})} \quad (2.8)$$

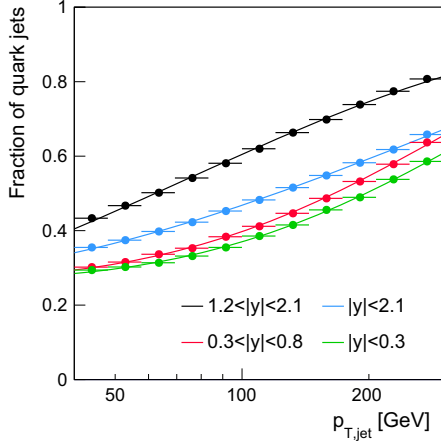
379 where p_{T0} is a reference transverse momentum at which $A = dn/dp_T^{\text{jet}}$, β is the logarithmic derivative of
380 dn/dp_T^{jet} at $p_T^{\text{jet}} = p_{T0}$. Then considering the different quark and gluon fractions as f_{q0} and $f_{g0} = 1 - f_{q0}$
381 respectively, the combined spectrum for quarks and gluons can be written as:

$$\frac{dN}{dp_T^{\text{jet}}} = A \left[f_{q0} \left(\frac{p_{T0}}{p_T^{\text{jet}}} \right)^{n_q + \beta_q \log(p_T^{\text{jet}}/p_{T0})} + (1 - f_{q0}) \left(\frac{p_{T0}}{p_T^{\text{jet}}} \right)^{n_g + \beta_g \log(p_T^{\text{jet}}/p_{T0})} \right] \quad (2.9)$$

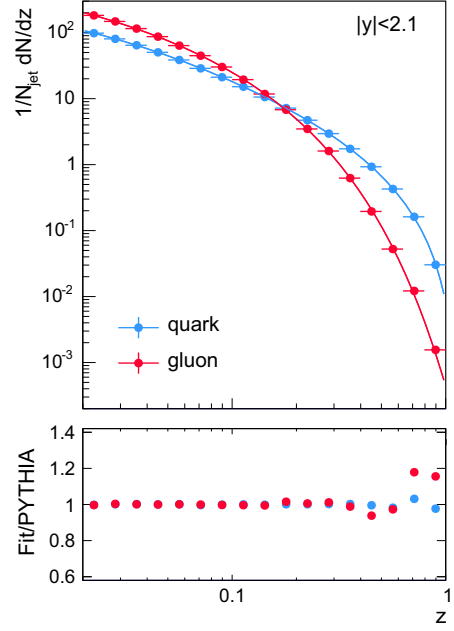
$$f_q(p_T^{\text{jet}}) = \frac{1}{1 + \left(\frac{1 - f_{q0}}{f_{q0}} \right) \left(\frac{p_{T0}}{p_T^{\text{jet}}} \right)^{\Delta n + \Delta \beta \log(p_T^{\text{jet}}/p_{T0})}} \quad (2.10)$$

382 where $\Delta n = n_g - n_q$ and $\Delta \beta = \beta_g - \beta_q$. The p_T dependence of the quark fraction along with the fit is shown
383 in Figure 2.11(a). The fragmentation functions can also be determined using final-state charged hadrons
384 within a $R = 0.4$ jet cone. These are fit to the form $D(z)$, with fits for the quark and gluon fragmentation
385 shown in Figure 2.11(b).

$$D(z) = a \times \frac{(1 + dz)^b}{(1 + ez)^c} \times e^{-fz} \quad (2.11)$$



(a) The jet quark fraction as a function of p_T^{jet} in different rapidity bins. The points are from PYTHIA8 simulations and the lines are fits to Equation 2.10.



(b) A comparison of the PYTHIA8 quark and gluon fragmentation. The solid lines are the fits from The jet quark fraction as a function of p_T^{jet} in different rapidity bins. The points are from PYTHIA8 simulations and the lines are fits to Equation 2.11.

Figure 2.11: Fits to quark fractions and fragmentation functions from PYTHIA8. Figure taken from [124]

386 For the quenched spectra, this model assumes a non-constant fractional shift given below as S . This
 387 approach is based on [131] and is used because of the inability of the constant fractional shift to explain the
 388 jet p_T dependence of measured R_{AA} .

$$S = s' \left(\frac{p_T^{\text{jet}}}{p_{T0}} \right)^\alpha \quad (2.12)$$

389 where α is an undetermined parameter and s' is the shift for a jet with $p_T^{\text{jet}} = p_{T0}$. This gives the following
 390 quenched high- p_T hadron spectra:

$$\begin{aligned} \frac{dN_Q}{dp_T^{\text{jet}}} = A & \left[f_{q0} \left(\frac{p_{T0}}{p_T^{\text{jet}} + S_q} \right)^{n_q + \beta_q \log((p_T^{\text{jet}} + S_q)/p_{T0})} \left(1 + \frac{dS_q}{dp_T^{\text{jet}}} \right) \right. \\ & \left. + (1 - f_{q0}) \left(\frac{p_{T0}}{p_T^{\text{jet}} + S_g} \right)^{n_g + \beta_g \log((p_T^{\text{jet}} + S_g)/p_{T0})} \left(1 + \frac{dS_g}{dp_T^{\text{jet}}} \right) \right] \end{aligned} \quad (2.13)$$

³⁹¹ Where the $(1 + dS/dp_T^{\text{jet}})$ term is a Jacobian to preserve the number of jets. Then the R_{AA} can be written as:

$$R_{\text{AA}} = f_q \left(\frac{1}{1 + S_q/p_T^{\text{jet}}} \right)^{n_q + \beta_q \log((p_T^{\text{jet}} + S_q)/p_{T0})} \frac{p_{T0}}{p_T^{\text{jet}}} \left(1 + \frac{dS_q}{dp_T^{\text{jet}}} \right) \times \quad (2.14)$$

$$(1 - f_q) \left(\frac{1}{1 + S_g/p_T^{\text{jet}}} \right)^{n_g + \beta_g \log((p_T^{\text{jet}} + S_g)/p_{T0})} \frac{p_{T0}}{p_T^{\text{jet}}} \left(1 + \frac{dS_g}{dp_T^{\text{jet}}} \right) \quad (2.15)$$

³⁹² where the flavor fraction is given by Equation 2.10. These can be fit to the measured ATLAS R_{AA} data as
³⁹³ shown in Figure 2.13(a) and the parameters s' and α can be extracted as shown in Figure 2.12.

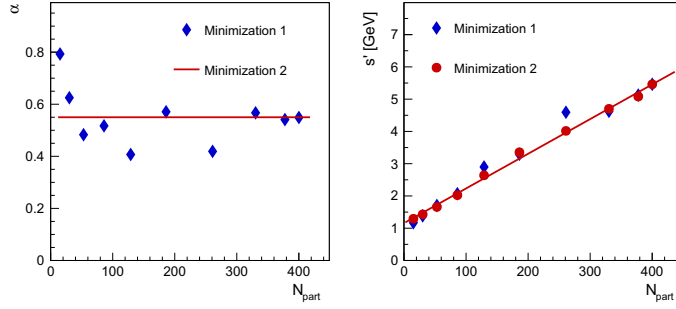
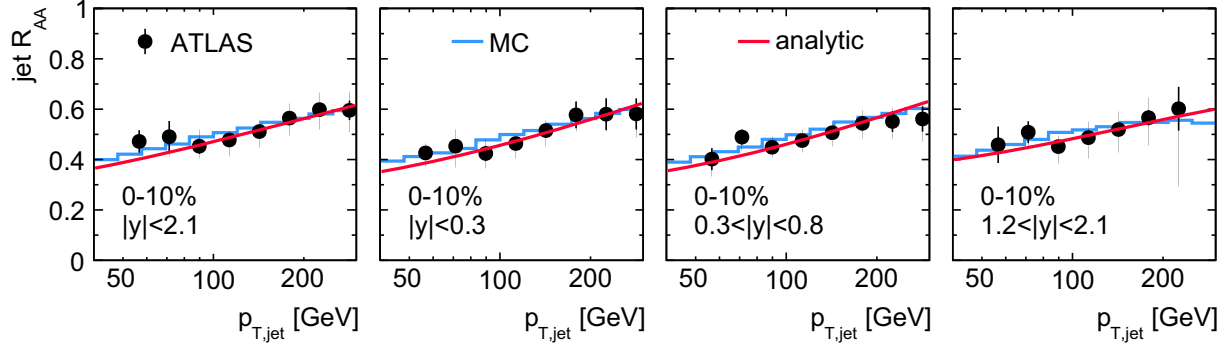
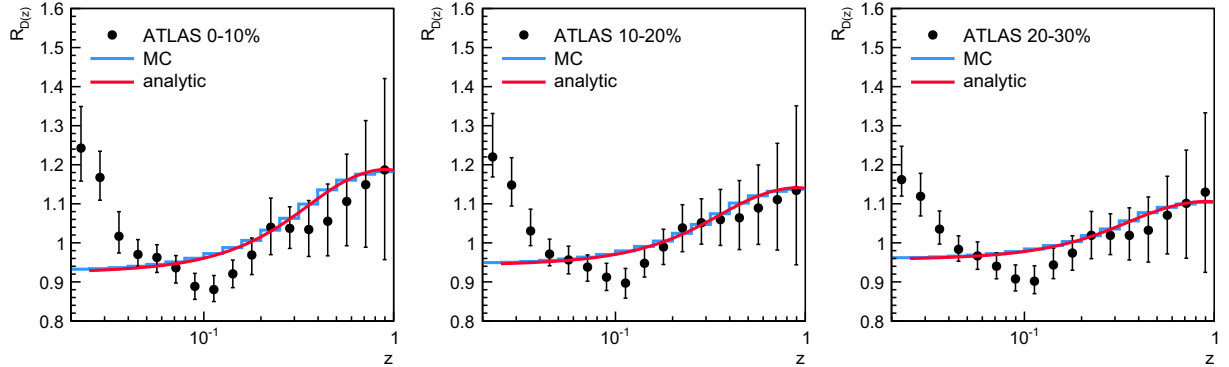


Figure 2.12: The extracted values of α and s' as a function of N_{part} . The first minimization shows fluctuations for α around 0.55, which was then fixed for the second minimization to give an s' that linearly depends on N_{part} . Figure taken from [124]

³⁹⁴ It can be seen that the analytic fits and the MC are in good agreement. While the fits agree with the data
³⁹⁵ by definition, the robustness of the model can be seen in that it describes the data with a single value for α
³⁹⁶ and a simple centrality dependent shift constant s' . Fits to the $D(z)$ distributions are shown in Figure 2.13(b)
³⁹⁷ and it can be seen that while the MC and analytic calculation agree well with each other, they are only
³⁹⁸ able to qualitatively capture some features of the data. The enhancement at high z can be explained by an
³⁹⁹ increased quark content of the jet spectrum and subsequent differential quenching for quark and gluon jets.
⁴⁰⁰ The low z enhancement on the other hand can be considered to be a result of a gluon radiation within the
⁴⁰¹ jet or a wake from the medium itself.



(a) A comparison of the R_{AA} as measured by ATLAS for central Pb+Pb collisions in [132], a MC calculation (blue) and the analytic calculation (red) in the EQ model with the extended power-law parameterization and a non-constant fractional energy loss. The different panels are different rapidity intervals.



(b) A comparison of the $R_{D(z)}$ as measured by ATLAS in [133], a MC calculation (blue) and the analytic calculation (red) in the EQ model with the extended power-law parameterization and a non-constant fractional energy loss. The different panels are different centrality intervals.

Figure 2.13: A comparison of measured data, MC, and the analytic calculation of the EQ model. Figure taken from [124]

402 2.5 Jet Fluid model

403 This discussion is based on the model introduced in Ref. [134]. This model considers the evolution of the jet
 404 and QGP in a coupled manner, considering the energy and transverse momentum exchange between them.
 405 In this picture, both the jet and medium are allowed to modify each other; the jet is modified via collisional
 406 and radiative processes while the medium evolves hydrodynamically and is modified because it picks up the
 407 energy lost by the jet.

408 The time evolution of the jet is given

$$f_i(\omega_i, k_{\text{T}i}^2, t) = \frac{dN_i(\omega_i k_{\text{T}i}^2, t)}{d\omega_i dk_{\text{T}i}^2} \quad (2.16)$$

409 where i is the type of parton, ω_i is its energy, and k_{T}^2 is its transverse momentum with respect to the jet axis.

410 Then the transport equations can be written in terms of :

$$\frac{df_j}{dt} = \hat{e}_j \frac{\partial f_j}{\partial \omega_j} + \frac{1}{4} \hat{q}_j \nabla_{k_{\text{T}}}^2 f_j \quad (2.17)$$

$$+ \sum_i \int d\omega_i dk_{\text{T}i}^2 \frac{d\tilde{\Gamma}_{i \rightarrow j}}{d\omega_j dk_{\text{T}j}^2 dt} f_i \quad (2.18)$$

$$- \sum_i \int d\omega_i dk_{\text{T}i}^2 \frac{d\tilde{\Gamma}_{j \rightarrow i}}{d\omega_{ij} dk_{\text{T}i}^2 dt} f_i \quad (2.19)$$

(2.20)

411 where the first term is the collisional energy loss, the second term is the transverse momentum broadening,
 412 and the last two terms are the medium induced gain and loss radiative processes respectively. The splitting
 413 processes are given by:

$$\frac{d\Gamma_{i \rightarrow j}}{d\omega_j dk_{\text{T}j}^2 dt} = \frac{2\alpha_S}{\pi} \hat{q}_g \frac{x P_{i \rightarrow j}(x)}{\omega_j k_{\text{T}j}^4} \sin^2 \left(\frac{t - t_i}{2\tau_f} \right) \quad (2.21)$$

414 where $P_{i \rightarrow j}$ is the vacuum splitting function for $i \rightarrow j$ with ω_j being the energy of the radiated parton, τ_f is
 415 the formation time of the radiated parton, and $k_{\text{T}j}$ is the transverse momentum of the radiated parton with
 416 respect to the parent parton. These transport Equations 2.17 can be solved numerically and agree with R_{AA}
 417 measurements [132, 135, 136]. The effects of the medium are included by considering the energy-momentum

418 conservation of the jet-QGP system $\partial_\mu [T_{\text{QGP}}^{\mu\nu} + T_{\text{jet}}^{\mu\nu}] = 0$. Then the source term $J^\nu(x)$ that describes the
 419 energy transfer between the jet and the medium can be defined as $J^\nu(x) \equiv -\partial_\mu T_{\text{jet}}^{\mu\nu}$, making the QGP
 420 evolution being given by

$$\partial_\mu T_{\text{QGP}}^{\mu\nu} = j^\nu \quad (2.22)$$

421 which characterizes the energy-momentum transfer between the jet and the QGP.

422 An important component of this model is the flow induced by jets. A snapshot of this is shown in
 423 Figure 2.14, where the evolution of the energy density of the medium can be seen in a sample event. A single
 424 jet travels through the QGP, and can be clearly seen in the lower panels after the energy of the medium has
 425 been subtracted out. The V shaped feature seen is the mach cone that is induced by the parton as it moves
 426 faster than the medium sound velocity.

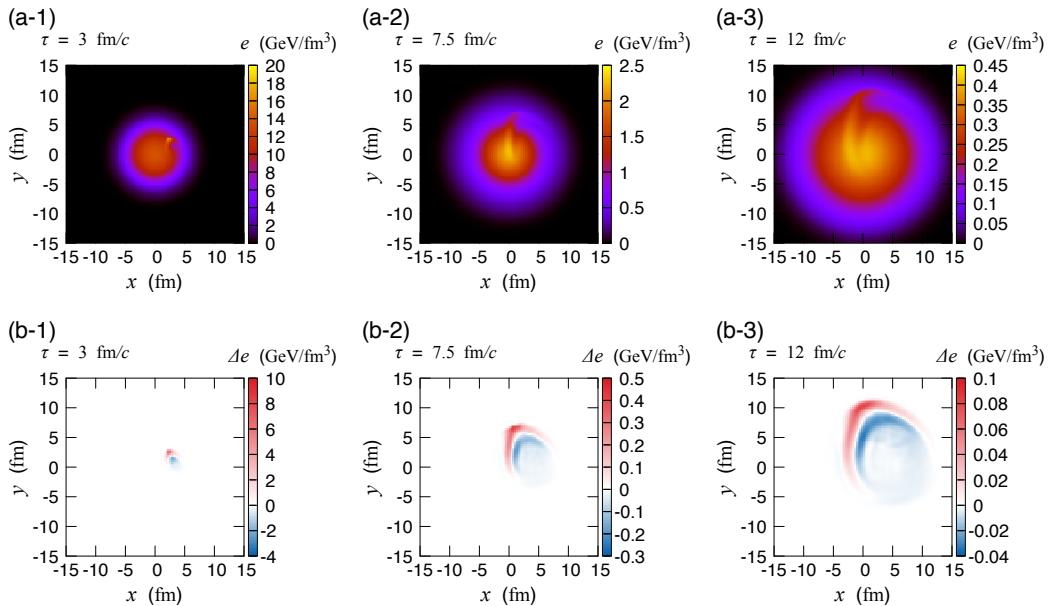


Figure 2.14: (Top) The time evolution of the energy density of the quark gluon plasma with a jet propagating through it. (Bottom) The time evolution of the energy density in the event after the energy density of the QGP has been subtracted out. Figure taken from [134].

427 The final jet energy has two components: the jet shower, and the hydrodynamic response. The former
 428 as discussed above comprises of the collisional energy loss, momentum broadening, and medium induced
 429 radiation. The latter includes the energy lost from the jet shower that thermalizes into the medium and
 430 induces conical flow, some of which is still in the jet cone. This compensates some of the energy lost in the

shower and can be seen in Figure 2.15. While the absolute amount of energy lost increases as a function of initial jet energy, the fractional energy loss decreases. Furthermore there is a cone size dependence once the hydrodynamic contributions are included. This is a result of the jet being highly collimated, such that while an increase in the size does not change the energy much, it does affect the hydrodynamic contribution from the medium.

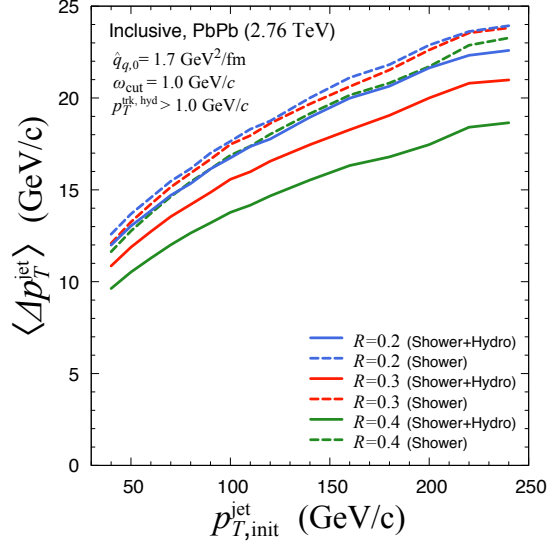


Figure 2.15: (Top) The energy lost by a jets of different radii as a function of their initial energy in central Pb+Pb collisions at $\sqrt{s_{\text{NN}}} = 2.76 \text{ TeV}$. Figure taken from [134].

The R_{AA} distributions constructed with this model and compared to data from CMS [135] are shown in Figure 2.16. Including the hydrodynamic contribution decreases the energy loss, hence increasing the R_{AA} value and inducing a cone size dependence to the R_{AA} .

The internal structure of the jet, i.e. how energy is spread within it, can be investigated using the jet shape variable, defined as a per-jet quantity as:

$$\rho_{\text{jet}} = \frac{1}{N_{\text{jet}}} \sum_{\text{jet}} \left[\frac{1}{p_{\text{T}}^{\text{jet}}} \frac{\sum_{\text{trk}} p_{\text{T}}^{\text{ch}}}{\delta r} \right] \quad (2.23)$$

where the sum is over all jets and for all tracks around a jet in an annulus with mean radius r from the jet axis. The modification in the jet structure then can be defined as:

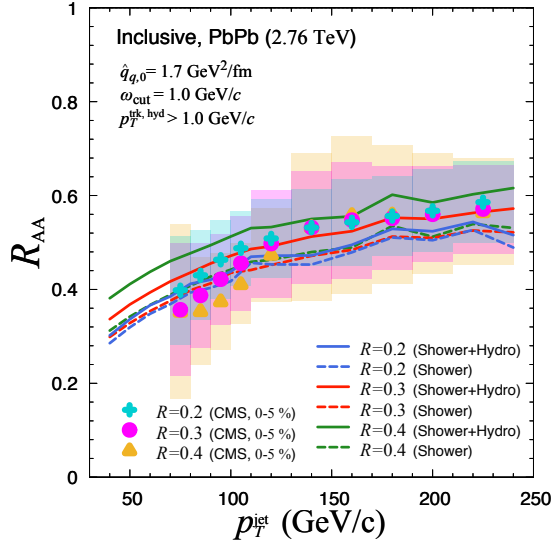


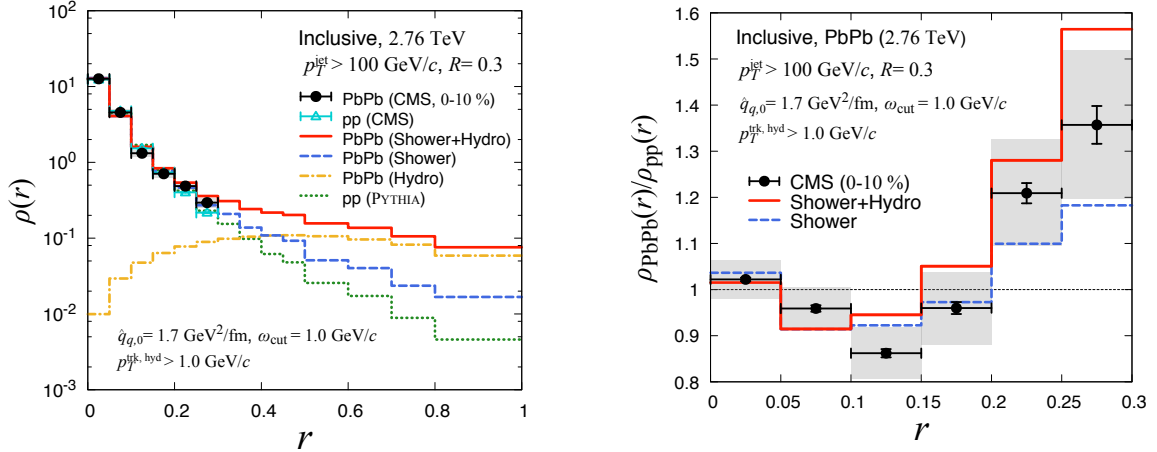
Figure 2.16: The nuclear modification factor R_{AA} as a function of jet p_T as determined by the Jet-Fluid model and compared to the data measured by CMS [135]. The different colors represent different sized jets, with the dashed lines showing the modeled R_{AA} without the hydro-contribution. There is good agreement within the large uncertainties in the data. Figure taken from [134].

$$R_{AA}^\rho = \frac{\rho_{AA}(r)}{\rho_{pp}(r)} \quad (2.24)$$

443 A comparison of the jet shape variable ρ and its modification R_{AA}^ρ to data measured by CMS is shown in
 444 Figure 2.17. The individual shower and hydro contributions are seen in Figure 2.17(a). These indicate that
 445 the shower contribution to the jet shape variable falls steeply as a function of distance from the jet axis
 446 while the hydro contribution is fairly constant at large distances. This is because the energy loss from the
 447 shower is carried away by the jet induced flow to large angles. The R_{AA}^ρ distribution in Figure 2.17(b), shows
 448 that the core is largely unmodified while the outer part of the jet is broadened. The hydro-contribution
 449 mainly has an effect at larger distances from the jet axis. This is consistent with the cone-size dependence
 450 seen in Figure 2.15.

451 2.6 Hybrid Model

452 This discussion is based on the work in Refs. [127, 138, 139] and describes jet quenching using a hybrid
 453 strong/weak model. It uses perturbative QCD to describe the weakly coupled hard process of jet production
 454 and holographic calculations of the energy loss of energetic probes to model the strong coupling between the



(a) The jet shape as measured by CMS for pp and central $Pb+Pb$ collisions [137] compared to the Jet Fluid model. The shower (blue) and hydro (orange) contributions to the jet shape are highlighted.

(b) The modification of the jet shape between pp and $Pb+Pb$ as measured by CMS [137] and compared to the Jet Fluid model. The dashed line shows the modeled modification without the hydro-contribution.

Figure 2.17: Fits to CMS data. Figures taken from [134].

455 probe and the plasma [140, 141]. This is a combination of approaches that focus on the following extreme
 456 limits: a weakly coupled system at unrealistically high temperatures that can be treated perturbatively
 457 [142, 143] and a system where the coupling constant is large at all energy scales and Gauge/string duality is
 458 applicable [144].

459 In this model, the jet evolves in space time with the lifetime of the parton in the shower being given by
 460 [145].

$$\tau = 2 \frac{E}{Q^2} \quad (2.25)$$

461 where Q is its virtuality and E its energy. This evolution is unaffected before the proper time at which the
 462 plasma hydrodynamizes, $\tau_{\text{hydro}} = 0.6$ fm. After this time, the jet-plasma interaction comes into play and the
 463 fragments evolve with the energy loss as:

$$\frac{1}{E_{\text{in}}} \frac{dE}{dx} = -\frac{4}{\pi} \frac{x^2}{x_{\text{stop}}^2} \frac{1}{\sqrt{x_{\text{stop}}^2 - x^2}} \quad (2.26)$$

464 where E_{in} is the initial energy of the parton prior to any quenching and x_{stop} is its stopping distance (jet
 465 thermalization distance). The stopping distance can be written as:

$$x_{\text{stop}} = \frac{1}{2\kappa_{\text{sc}}} \frac{E_{\text{in}}^{1/3}}{T^{4/3}} \quad (2.27)$$

466 where κ_{sc} is a dimensionless free parameter associated to the strong coupling and is used to fit to the
 467 data. The energy loss is characterized by the strong x^2 dependence for $x \ll x_{\text{stop}}$. Furthermore, when x is
 468 comparable to x_{stop} , dE/dx depends nontrivially on E_{in} and x , diverging for $x \rightarrow x_{\text{stop}}$ and $E \rightarrow 0$. The
 469 shower is then embedded into a hydrodynamic description of the QGP from Ref. [146], and the energy
 470 loss expressions are integrated for each parton, from the time it is produced to the time that it splits. The
 471 splitting probabilities are taken to be independent of the medium, depending only on the initial energy of the
 472 daughter partons. These further lose energy as they propagate through the QGP and split. Then the total
 473 energy lost by a parton is dependent on the history of splitting and propagation of its parents, grandparents
 474 and so on and so forth.

475 The partons further experience kicks transverse to their direction of motion, a phenomena called transverse
 476 momentum broadening. This effect is mainly experienced by softer partons that are much more affected
 477 by the angular narrowing effects of energy loss, making most measured observables insensitive to the size
 478 of this kick. This is directly related to wider jets losing more energy than narrower ones. The wake left
 479 in the medium from the partons depositing momentum in the QGP as they propagate through it lends a
 480 non-trivial impact to the model predictions. This wake moves in the direction of the jet and is impossible to
 481 separate out in experiments, making its inclusion to any model vital. This wake results in a perturbation
 482 to the hydrodynamic background, resulting in corrections to the final state hadron spectra. This effect is
 483 particularly important for jet substructure observables like jet fragmentation and jet shapes [139].

484 A screening effect recently included in the hybrid model is based considering the resolving power of the
 485 QGP [138]. As depicted in Figure 2.18, the QGP will only resolve daughter partons of a splitting after they
 486 are separated by a certain distance L_{res} . It is only after they are resolved that they will be allowed them to
 487 lose energy independent of each other. This delayed quenching results in an enhancement of softer partons at
 488 larger angles from the jet axis compared to the case where the daughter partons are resolved immediately
 489 after they split from the parent parton. The L_{res} parameter has the constraint $1/(\pi T) < L_{\text{res}} < 2/(p_{\text{T}} T)$
 490 based on the Debye screening length for the plasma, i.e. the length at which the QGP is able to resolve and
 491 screen color charges.

492 The free parameter κ_{sc} is determined by fitting to jet R_{AA} data from CMS [135] as shown in Figure 2.19.
 493 It can be seen that including the L_{res} parameter does not really affect the jet R_{AA} prediction. The dependence

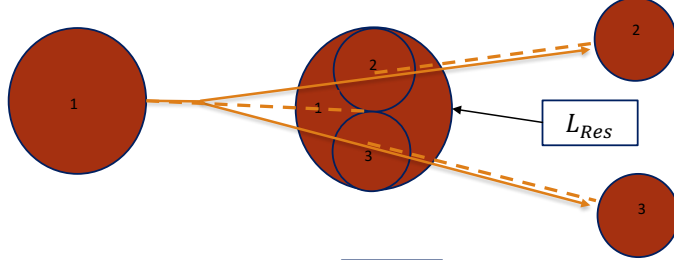


Figure 2.18: A schematic illustrating the resolving power of the QGP. The daughter partons 2 and 3 that come from 1 need to be separated by L_{res} before they are treated individually by the plasma. Prior to that separation, they are treated as one effective parton. Figure taken from [138].

494 of the R_{AA} on the size of the jet radius can be seen. This is consistent with the expectation that wider jets
 495 lose more energy.

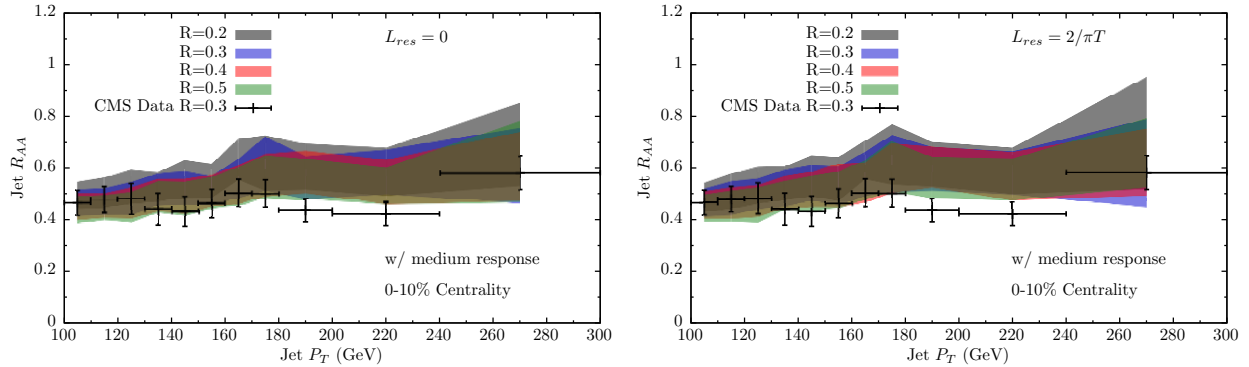
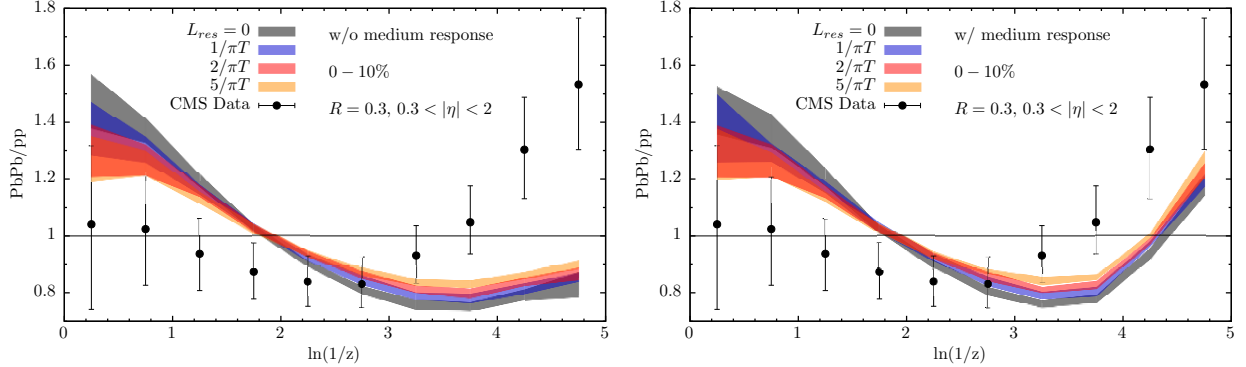


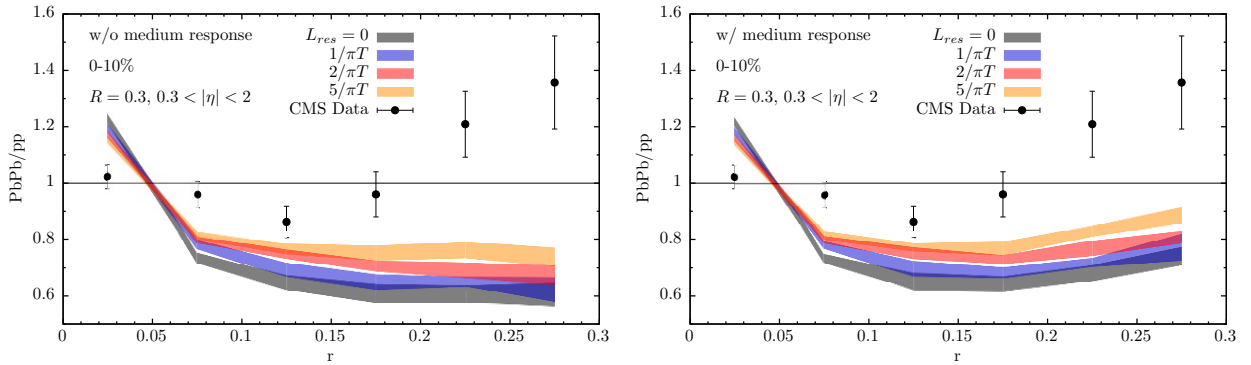
Figure 2.19: The hybrid model without (left) and with (right) the L_{res} parameter, compared to the jet R_{AA} as a function of jet p_T in two centrality intervals as measured in Ref. [135]. The different colors correspond to different jet radii. The Hybrid Model is fit to the 100–110 GeV point from the data, giving rise to the colored bands. Figure taken from [138].

496 Fixing the κ_{sc} parameter allows for predictions of other jet measurements like jet fragmentation and
 497 jet shape. Figures 2.20(a) and 2.20(b) show a comparison of the measured and modeled values of the
 498 modifications to the jet fragmentation and jet shape respectively. The model has also been compared to
 499 measurements done by ATLAS, ALICE, and STAR [120, 136, 147] []

500 Here it can be seen that adding a medium response and a non-zero L_{res} parameter affects the prediction.
 501 While the hard fragments (see Figure ??) are unaffected by the medium response, including the soft particles
 502 from the wake compensates some of the suppression of soft fragments in Pb+Pb compared to pp collisions.
 503 Moreover, including the L_{res} parameter further compensates the suppression for soft fragments, while reducing
 504 the enhancement of the hard fragments. This is a result of allowing more hadrons carrying a smaller fraction
 505 of the jet energy (low z , high $(\ln(1/z))$) to survive into the final state. The jet shape observable (see Figure ??)



(a) The modification to the jet fragmentation from pp to $Pb+Pb$ as a function of $\ln(1/z)$ as measured in Ref. [148] compared to the predictions of the hybrid model. The predictions are shown without (left) and with (right) the effect of the wake from the QGP responding to the jet. The different colors correspond to different L_{res} parameters. Figure taken from [138].



(b) The modification to the jet shape from pp to $Pb+Pb$ as a function of r as measured in Ref. [137] compared to the predictions of the hybrid model. The predictions are shown without (left) and with (right) the effect of the wake from the QGP responding to the jet. The different colors correspond to different L_{res} parameters. Figure taken from [138].

Figure 2.20: A comparison of measured data, MC, and the analytic calculation of the EQ model. Figure taken from [124]

506 quantifies the radial distribution of energy in terms of annuli around the jet axis. It can be seen that
507 introducing the L_{res} parameter enhances the probability to find final state hadrons at larger distances from
508 the jet axis. The jet core ($r < 0.05$) is also affected, with the depletion only slowly evolving with an increasing
509 L_{res} . One must be careful before making conclusions though, since these modifications are made between jets
510 that are quenched (in Pb+Pb) and unquenched (in pp). Taking into account the fact that wider jets lose
511 more energy and that the jet spectrum rapidly falls off, there is a bias for finding narrower quenched jets
512 than unquenched jets. This makes the jet shape after quenching narrower in Pb+Pb compared to pp . While
513 the model is not fully able to capture the features in the data, including the medium response moves it in
514 the correct direction. It can be suggested that the model is missing a description of the medium induced
515 modification to the hadronization process or that the wakes in the plasma are not equilibrating.

Bibliography

- 516 [1] G. Roland, K. Safarik and P. Steinberg, *Heavy-ion collisions at the LHC*, Prog. Part. Nucl. Phys. **77**
517 (2014) 70 (cit. on p. 1).
- 518 [2] M. K. Gaillard, P. D. Grannis and F. J. Sciulli, *The Standard model of particle physics*, Rev. Mod.
519 Phys. **71** (1999) S96, arXiv: [hep-ph/9812285 \[hep-ph\]](#) (cit. on p. 1).
- 520 [3] Wikimedia Commons, *Standard Model of Elementary Particles*, (2006), URL: https://en.wikipedia.org/wiki/Standard_Model (cit. on p. 1).
- 521 [4] J Beringer et al., *Review of Particle Physics, 2012-2013. Review of Particle Properties*, Phys. Rev. D
522 **86** (2012) 010001 (cit. on pp. 2, 3).
- 523 [5] D. J. Gross and F. Wilczek, *Ultraviolet Behavior of Non-Abelian Gauge Theories*, Phys. Rev. Lett. **30**
524 (26 1973) 1343, URL: <https://link.aps.org/doi/10.1103/PhysRevLett.30.1343> (cit. on p. 4).
- 525 [6] D. J. Gross and F. Wilczek, *Asymptotically Free Gauge Theories. I*, Phys. Rev. D **8** (10 1973) 3633,
526 URL: <https://link.aps.org/doi/10.1103/PhysRevD.8.3633> (cit. on p. 4).
- 527 [7] A. Deur et al., *High precision determination of the Q^2 evolution of the Bjorken Sum*, Phys. Rev. D**90**
528 (2014) 012009, arXiv: [1405.7854 \[nucl-ex\]](#) (cit. on p. 4).
- 529 [8] J. H. Kim et al., *A Measurement of $\alpha_s(Q^2)$ from the Gross-Llewellyn Smith sum rule*, Phys. Rev. Lett.
530 **81** (1998) 3595, arXiv: [hep-ex/9808015 \[hep-ex\]](#) (cit. on p. 4).
- 531 [9] G. Altarelli et al., *Determination of the Bjorken sum and strong coupling from polarized structure
functions*, Nucl. Phys. **B496** (1997) 337, arXiv: [hep-ph/9701289 \[hep-ph\]](#) (cit. on p. 4).
- 532 [10] H. W. Kendall, *Deep inelastic scattering: Experiments on the proton and the observation of scaling*,
533 Rev. Mod. Phys. **63** (3 1991) 597 (cit. on p. 4).
- 534 [11] A. L. Kataev, G. Parente and A. V. Sidorov, *Improved fits to the xF_3 CCFR data at the next-to-next-to-
535 leading order and beyond*, Phys. Part. Nucl. **34** (2003) 20, [Erratum: Phys. Part. Nucl.38,no.6,827(2007)],
536 arXiv: [hep-ph/0106221 \[hep-ph\]](#) (cit. on p. 4).
- 537
- 538

- 539 [12] S. Alekhin, J. Blumlein and S. Moch, *Parton Distribution Functions and Benchmark Cross Sections*
 540 *at NNLO*, Phys. Rev. **D86** (2012) 054009, arXiv: [1202.2281 \[hep-ph\]](#) (cit. on p. 4).
- 541 [13] S. Alekhin, J. Blumlein and S.-O. Moch, *ABM news and benchmarks*, PoS **DIS2013** (2013) 039, arXiv:
 542 [1308.5166 \[hep-ph\]](#) (cit. on p. 4).
- 543 [14] J. Blumlein, H. Bottcher and A. Guffanti, *Non-singlet QCD analysis of deep inelastic world data at*
 544 $O(\alpha_s^3)$, Nucl. Phys. **B774** (2007) 182, arXiv: [hep-ph/0607200 \[hep-ph\]](#) (cit. on p. 4).
- 545 [15] H1 Collaboration, *Three- and Four-jet Production at Low x at HERA*, Eur. Phys. J. **C54** (2008) 389,
 546 arXiv: [0711.2606 \[hep-ex\]](#) (cit. on p. 4).
- 547 [16] ZEUS Collaboration, *Forward-jet production in deep inelastic ep scattering at HERA*, Eur. Phys. J.
 548 **C52** (2007) 515, arXiv: [0707.3093 \[hep-ex\]](#) (cit. on p. 4).
- 549 [17] ZEUS Collaboration, *Multi-jet cross-sections in charged current $e^\pm p$ scattering at HERA*, Phys. Rev.
 550 **D78** (2008) 032004, arXiv: [0802.3955 \[hep-ex\]](#) (cit. on p. 4).
- 551 [18] ZEUS Collaboration, *Inclusive dijet cross sections in neutral current deep inelastic scattering at HERA*,
 552 Eur. Phys. J. **C70** (2010) 965, arXiv: [1010.6167 \[hep-ex\]](#) (cit. on p. 4).
- 553 [19] ZEUS Collaboration, *Inclusive-jet cross sections in NC DIS at HERA and a comparison of the kT ,*
 554 *anti- kT and SIScone jet algorithms*, Phys. Lett. **B691** (2010) 127, arXiv: [1003.2923 \[hep-ex\]](#) (cit. on
 555 p. 4).
- 556 [20] H1 Collaboration, *Jet Production in ep Collisions at High Q^2 and Determination of α_s* , Eur. Phys. J.
 557 **C65** (2010) 363, arXiv: [0904.3870 \[hep-ex\]](#) (cit. on p. 4).
- 558 [21] E. D. Bloom et al., *High-Energy Inelastic $e - p$ Scattering at 6° and 10°* , Phys. Rev. Lett. **23** (16
 559 1969) 930, URL: <https://link.aps.org/doi/10.1103/PhysRevLett.23.930> (cit. on p. 4).
- 560 [22] M. Breidenbach et al., *Observed Behavior of Highly Inelastic Electron-Proton Scattering*, Phys. Rev.
 561 Lett. **23** (16 1969) 935, URL: <https://link.aps.org/doi/10.1103/PhysRevLett.23.935> (cit. on
 562 p. 4).
- 563 [23] J. D. Bjorken, *Asymptotic Sum Rules at Infinite Momentum*, Phys. Rev. **179** (5 1969) 1547, URL:
 564 <https://link.aps.org/doi/10.1103/PhysRev.179.1547> (cit. on p. 4).
- 565 [24] K. Nishijima, *BRS invariance, asymptotic freedom and color confinement (a review)*, Czechoslovak
 566 Journal of Physics **46** (1996) 1, ISSN: 1572-9486, URL: <https://doi.org/10.1007/BF01692238>
 567 (cit. on p. 4).

- 568 [25] K. G. Wilson, *Confinement of quarks*, Phys. Rev. D **10** (8 1974) 2445, URL: <https://link.aps.org/doi/10.1103/PhysRevD.10.2445> (cit. on p. 4).
- 570 [26] W. Buchmuller, *Fine- and hyperfine structure of quarkonia*, Physics Letters B **112** (1982) 479 ,
571 ISSN: 0370-2693, URL: <http://www.sciencedirect.com/science/article/pii/0370269382908541>
572 (cit. on p. 4).
- 573 [27] J. Kogut, D. Sinclair and L. Susskind, *A quantitative approach to low-energy quantum chromodynamics*,
574 Nuclear Physics B **114** (1976) 199 , ISSN: 0550-3213, URL: <http://www.sciencedirect.com/science/article/pii/0550321376905861> (cit. on p. 4).
- 576 [28] N. Isgur and J. Paton, *Flux-tube model for hadrons in QCD*, Phys. Rev. D **31** (11 1985) 2910, URL:
577 <https://link.aps.org/doi/10.1103/PhysRevD.31.2910> (cit. on p. 4).
- 578 [29] M. Faber, J. Greensite and OlejnkaS, *Casimir scaling from center vortices: Towards an understanding
579 of the adjoint string tension*, Phys. Rev. D **57** (4 1998) 2603, URL: <https://link.aps.org/doi/10.1103/PhysRevD.57.2603> (cit. on p. 4).
- 581 [30] G. S. Bali, *Casimir scaling of SU(3) static potentials*, Phys. Rev. D **62** (11 2000) 114503, URL:
582 <https://link.aps.org/doi/10.1103/PhysRevD.62.114503> (cit. on p. 4).
- 583 [31] J. B. Kogut, *The lattice gauge theory approach to quantum chromodynamics*, Rev. Mod. Phys. **55** (3
584 1983) 775, URL: <https://link.aps.org/doi/10.1103/RevModPhys.55.775> (cit. on p. 4).
- 585 [32] D. Zwanziger, *No Confinement without Coulomb Confinement*, Phys. Rev. Lett. **90** (10 2003) 102001,
586 URL: <https://link.aps.org/doi/10.1103/PhysRevLett.90.102001> (cit. on p. 4).
- 587 [33] A. Jaffe and E. Witten, *Yang-Mills and Mass Gap*, <http://www.claymath.org/millennium-problems/yang-mills-and-mass-gap> (cit. on p. 4).
- 589 [34] E. V. Shuryak, *Quantum chromodynamics and the theory of superdense matter*, Physics Reports **61**
590 (1980) 71 , ISSN: 0370-1573 (cit. on pp. 4, 8).
- 591 [35] J. C. Collins and M. J. Perry, *Superdense Matter: Neutrons or Asymptotically Free Quarks?*, Phys.
592 Rev. Lett. **34** (21 1975) 1353 (cit. on pp. 4, 6).
- 593 [36] A. D. Linde, *Phase transitions in gauge theories and cosmology*, Reports on Progress in Physics **42**
594 (1979) 389 (cit. on p. 4).
- 595 [37] LIGO/VIRGO Collaboration, *GW170817: Observation of Gravitational Waves from a Binary Neutron
596 Star Inspiral*, Phys. Rev. Lett. **119** (16 2017) 161101, URL: <https://link.aps.org/doi/10.1103/PhysRevLett.119.161101> (cit. on p. 4).

- 598 [38] S. Han and A. W. Steiner, *Tidal deformability with sharp phase transitions in (binary) neutron stars*,
 599 *Phys. Rev.* **D99** (2019) 083014, arXiv: [1810.10967 \[nucl-th\]](https://arxiv.org/abs/1810.10967) (cit. on p. 4).
- 600 [39] J.-E. Christian, A. Zacchi and J. Schaffner-Bielich, *Signals in the tidal deformability for phase*
 601 *transitions in compact stars with constraints from GW170817*, *Phys. Rev. D* **99** (2 2019) 023009, URL:
 602 <https://link.aps.org/doi/10.1103/PhysRevD.99.023009> (cit. on p. 4).
- 603 [40] E. R. Most et al., *Signatures of Quark-Hadron Phase Transitions in General-Relativistic Neutron-Star*
 604 *Mergers*, *Phys. Rev. Lett.* **122** (6 2019) 061101, URL: <https://link.aps.org/doi/10.1103/PhysRevLett.122.061101> (cit. on p. 4).
- 605 [41] A. Bauswein, H.-T. Janka, K. Hebeler and A. Schwenk, *Equation-of-state dependence of the gravitational-*
 606 *wave signal from the ring-down phase of neutron-star mergers*, *Phys. Rev. D* **86** (6 2012) 063001, URL:
 607 <https://link.aps.org/doi/10.1103/PhysRevD.86.063001> (cit. on p. 5).
- 608 [42] A. Bauswein et al., *Identifying a First-Order Phase Transition in Neutron-Star Mergers through*
 609 *Gravitational Waves*, *Phys. Rev. Lett.* **122** (6 2019) 061102, URL: <https://link.aps.org/doi/10.1103/PhysRevLett.122.061102> (cit. on p. 5).
- 610 [43] S. Borsanyi et al., *Is there still any T_c mystery in lattice QCD? Results with physical masses in the*
 611 *continuum limit III*, *JHEP* **09** (2010) 073, arXiv: [1005.3508 \[hep-lat\]](https://arxiv.org/abs/1005.3508) (cit. on p. 5).
- 612 [44] A. S. Kronfeld, *Twenty-first Century Lattice Gauge Theory: Results from the QCD Lagrangian*, *Ann.*
 613 *Rev. Nucl. Part. Sci.* **62** (2012) 265, arXiv: [1203.1204 \[hep-lat\]](https://arxiv.org/abs/1203.1204) (cit. on p. 5).
- 614 [45] J. W. Harris and B. Muller, *The search for the quark-gluon plasma*, *Annual Review of Nuclear and*
 615 *Particle Science* **46** (1996) 71, eprint: <https://doi.org/10.1146/annurev.nucl.46.1.71>, URL:
 616 <https://doi.org/10.1146/annurev.nucl.46.1.71> (cit. on p. 5).
- 617 [46] PHENIX Collaboration, *Enhanced Production of Direct Photons in Au + Au Collisions at $\sqrt{s_{NN}} =$*
 618 *200 GeV and Implications for the Initial Temperature*, *Phys. Rev. Lett.* **104** (13 2010) 132301 (cit. on
 619 p. 5).
- 620 [47] ALICE Collaboration, *Direct photon production in Pb–Pb collisions at $s_{NN}=2.76$ TeV*, *Physics Letters*
 621 *B* **754** (2016) 235 , ISSN: 0370-2693 (cit. on p. 5).
- 622 [48] Z. Fodor and S. Katz, *Critical point of QCD at finite T and μ , lattice results for physical quark masses*,
 623 *Journal of High Energy Physics* **2004** (2004) 050 (cit. on p. 5).
- 624 [49] STAR Collaboration, *Experimental and theoretical challenges in the search for the quark-gluon plasma: The STAR Collaboration's critical assessment of the evidence from RHIC collisions*, *Nuclear Physics*
 625 *A* **757** (2005) 102 , First Three Years of Operation of RHIC, ISSN: 0375-9474 (cit. on p. 5).

- [50] ALICE Collaboration, *Production of light nuclei and anti-nuclei in pp and Pb-Pb collisions at energies available at the CERN Large Hadron Collider*, *Phys. Rev. C* **93** (2 2016) 024917 (cit. on p. 5).
- [51] PHENIX Collaboration, *Single identified hadron spectra from $\sqrt{s_{NN}} = 130$ GeV Au + Au collisions*, *Phys. Rev. C* **69** (2 2004) 024904 (cit. on p. 5).
- [52] BRAHMS Collaboration, *Centrality dependent particle production at $y = 0$ and $y \geq 1$ in Au+Au collisions at $\sqrt{s_{NN}} = 200$ GeV*, *Phys. Rev. C* **72** (1 2005) 014908 (cit. on p. 5).
- [53] PHOBOS Collaboration, *Identified hadron transverse momentum spectra in Au+Au collisions at $\sqrt{s_{NN}} = 62.4$ GeV*, *Phys. Rev. C* **75** (2 2007) 024910 (cit. on p. 5).
- [54] ALICE Collaboration, *Centrality dependence of π , K , and p production in Pb-Pb collisions at $\sqrt{s_{NN}} = 2.76$ TeV*, *Phys. Rev. C* **88** (4 2013) 044910 (cit. on p. 5).
- [55] U. Heinz and R. Snellings, *Collective flow and viscosity in relativistic heavy-ion collisions*, Annual Review of Nuclear and Particle Science **63** (2013) 123 (cit. on p. 6).
- [56] M. Gyulassy, ‘The QGP Discovered at RHIC’, *Structure and Dynamics of Elementary Matter*, ed. by W. Greiner, M. G. Itkis, J. Reinhardt and M. C. Gucu, Springer Netherlands, 2004 159, ISBN: 978-1-4020-2705-5 (cit. on p. 6).
- [57] W. Busza et al., *Heavy Ion Collisions: The Big Picture, and the Big Questions*, *Ann. Rev. Nucl. Part. Sci.* **68** (2018) 339, arXiv: [1802.04801 \[hep-ph\]](#) (cit. on pp. 6–8).
- [58] A. Ster, T. Csorgo and B. Lorstad, *The Reconstructed final state of Pb + Pb 158-GeV/A reactions from spectra and correlation data of NA49, NA44 and WA98*, *Nucl. Phys. A* **661** (1999) 419, arXiv: [hep-ph/9907338 \[hep-ph\]](#) (cit. on p. 6).
- [59] A. M. Poskanzer et al., *Centrality dependence of directed and elliptic flow at the SPS*, *Nucl. Phys. A* **661** (1999) 341, arXiv: [nucl-ex/9906013 \[nucl-ex\]](#) (cit. on p. 6).
- [60] C. Pinkenburg et al., *Elliptic flow: Transition from out-of-plane to in-plane emission in Au + Au collisions*, *Phys. Rev. Lett.* **83** (1999) 1295, arXiv: [nucl-ex/9903010 \[nucl-ex\]](#) (cit. on p. 6).
- [61] ATLAS Collaboration, *Measurement of the azimuthal anisotropy of charged particles produced in $\sqrt{s_{NN}} = 5.02$ TeV Pb+Pb collisions with the ATLAS detector*, *Eur. Phys. J. C* **78** (2018) 997, arXiv: [1808.03951 \[nucl-ex\]](#) (cit. on p. 6).
- [62] PHENIX Collaboration, *Elliptic Flow of Identified Hadrons in Au + Au Collisions at $\sqrt{s_{NN}} = 200$ GeV*, *Phys. Rev. Lett.* **91** (18 2003) 182301 (cit. on p. 6).

- 658 [63] CMS Collaboration, *Non-Gaussian elliptic-flow fluctuations in PbPb collisions at $\sqrt{s_{NN}} = 5.02$ TeV*,
 659 *Phys. Lett.* **B789** (2019) 643, arXiv: [1711.05594 \[nucl-ex\]](#) (cit. on p. 6).
- 660 [64] ALICE Collaboration, *Anisotropic Flow of Charged Particles in Pb-Pb Collisions at $\sqrt{s_{NN}} = 5.02$*
 661 *TeV, Phys. Rev. Lett.* **116** (13 2016) 132302 (cit. on p. 6).
- 662 [65] M. Connors, C. Nattrass, R. Reed and S. Salur, *Jet measurements in heavy ion physics*, *Rev. Mod.*
 663 *Phys.* **90** (2 2018) 025005 (cit. on p. 6).
- 664 [66] A. M. Poskanzer and S. A. Voloshin, *Methods for analyzing anisotropic flow in relativistic nuclear*
 665 *collisions*, *Phys. Rev.* **C58** (1998) 1671, arXiv: [nucl-ex/9805001 \[nucl-ex\]](#) (cit. on p. 6).
- 666 [67] S. A. Voloshin, A. M. Poskanzer and R. Snellings, *Collective phenomena in non-central nuclear*
 667 *collisions*, *Landolt-Bornstein* **23** (2010) 293, arXiv: [0809.2949 \[nucl-ex\]](#) (cit. on pp. 6, 7).
- 668 [68] D. Teaney, J. Lauret and E. V. Shuryak, *A Hydrodynamic description of heavy ion collisions at the*
 669 *SPS and RHIC*, (2001), arXiv: [nucl-th/0110037 \[nucl-th\]](#) (cit. on p. 6).
- 670 [69] T. Hirano, U. Heinz, D. Kharzeev, R. Lacey and Y. Nara, *Hadronic dissipative effects on elliptic*
 671 *flow in ultrarelativistic heavy-ion collisions*, *Physics Letters B* **636** (2006) 299 , ISSN: 0370-2693, URL:
 672 <http://www.sciencedirect.com/science/article/pii/S0370269306003996> (cit. on p. 6).
- 673 [70] ALICE Collaboration, *Higher harmonic anisotropic flow measurements of charged particles in Pb-Pb*
 674 *collisions at $\sqrt{s_{NN}}=2.76$ TeV*, *Phys. Rev. Lett.* **107** (2011) 032301, arXiv: [1105.3865 \[nucl-ex\]](#)
 675 (cit. on p. 7).
- 676 [71] H. Niemi, K. J. Eskola and R. Paatelainen, *Event-by-event fluctuations in a perturbative QCD*
 677 *+ saturation + hydrodynamics model: Determining QCD matter shear viscosity in ultrarelativistic*
 678 *heavy-ion collisions*, *Phys. Rev.* **C93** (2016) 024907, arXiv: [1505.02677 \[hep-ph\]](#) (cit. on p. 7).
- 679 [72] BRAHMS Collaboration, *Quark-gluon plasma and color glass condensate at RHIC? The perspective*
 680 *from the BRAHMS experiment*, *Nuclear Physics A* **757** (2005) 1 , First Three Years of Opera-
 681 *tion of RHIC*, ISSN: 0375-9474, URL: <http://www.sciencedirect.com/science/article/pii/S0375947405002770> (cit. on p. 7).
- 683 [73] M. Gyulassy and L. McLerran, *New forms of QCD matter discovered at RHIC*, *Nuclear Physics A*
 684 **750** (2005) 30 , Quark-Gluon Plasma. New Discoveries at RHIC: Case for the Strongly Interacting
 685 Quark-Gluon Plasma. Contributions from the RBRC Workshop held May 14-15, 2004, ISSN: 0375-9474,
 686 URL: <http://www.sciencedirect.com/science/article/pii/S0375947404011480> (cit. on p. 7).

- [687] [74] PHENIX Collaboration, *Transverse energy production and charged-particle multiplicity at midrapidity in various systems from $\sqrt{s_{NN}} = 7.7$ to 200 GeV*, *Phys. Rev. C* **93** (2 2016) 024901, URL: <https://link.aps.org/doi/10.1103/PhysRevC.93.024901> (cit. on p. 8).
- [688]
- [689]
- [690] [75] ALICE Collaboration, *Measurement of transverse energy at midrapidity in Pb-Pb collisions at $\sqrt{s_{NN}} = 2.76$ TeV*, *Phys. Rev. C* **94** (3 2016) 034903, URL: <https://link.aps.org/doi/10.1103/PhysRevC.94.034903> (cit. on p. 8).
- [691]
- [692]
- [693] [76] CMS Collaboration, *Measurement of the Pseudorapidity and Centrality Dependence of the Transverse Energy Density in Pb-Pb Collisions at $\sqrt{s_{NN}} = 2.76$ TeV*, *Phys. Rev. Lett.* **109** (15 2012) 152303, URL: <https://link.aps.org/doi/10.1103/PhysRevLett.109.152303> (cit. on p. 8).
- [694]
- [695]
- [696] [77] F. Karsch, ‘Lattice QCD at High Temperature and Density’, *Lectures on Quark Matter*, ed. by W. Plessas and L. Mathelitsch, Springer Berlin Heidelberg, 2002 209, ISBN: 978-3-540-45792-3, URL: https://doi.org/10.1007/3-540-45792-5_6 (cit. on p. 8).
- [697]
- [698]
- [699] [78] A. Bazavov et al., *Equation of state in (2 + 1)-flavor QCD*, *Phys. Rev. D* **90** (9 2014) 094503, URL: <https://link.aps.org/doi/10.1103/PhysRevD.90.094503> (cit. on p. 8).
- [700]
- [701] [79] R. Glauber, *Lectures in theoretical physics*, ed. WE Brittin and LG Dunham, Interscience, New York **1** (1959) 315 (cit. on p. 9).
- [702]
- [703] [80] R. Glauber et al., *Lectures in theoretical physics*, 1959 (cit. on p. 9).
- [704] [81] H. D. Vries, C. D. Jager and C. D. Vries, *Nuclear charge-density-distribution parameters from elastic electron scattering*, *Atomic Data and Nuclear Data Tables* **36** (1987) 495 , ISSN: 0092-640X (cit. on pp. 9, 10).
- [705]
- [706]
- [707] [82] M. L. Miller, K. Reygers, S. J. Sanders and P. Steinberg, *Glauber Modeling in High-Energy Nuclear Collisions*, *Annual Review of Nuclear and Particle Science* **57** (2007) 205 (cit. on pp. 9, 10, 12, 23).
- [708]
- [709] [83] B. Alver, M. Baker, C. Loizides and P. Steinberg, *The PHOBOS Glauber Monte Carlo*, (2008), arXiv: [0805.4411 \[nucl-ex\]](https://arxiv.org/abs/0805.4411) (cit. on p. 9).
- [710]
- [711] [84] D. Kharzeev and M. Nardi, *Hadron production in nuclear collisions at RHIC and high density QCD*, *Phys. Lett. B* **507** (2001) 121, arXiv: [nucl-th/0012025 \[nucl-th\]](https://arxiv.org/abs/hep-ph/0012025) (cit. on p. 11).
- [712]
- [713] [85] A. Bialas, M. Bleszynski and W. Czyz, *Multiplicity Distributions in Nucleus-Nucleus Collisions at High-Energies*, *Nucl. Phys.* **B111** (1976) 461 (cit. on p. 11).
- [714]
- [715] [86] ATLAS Collaboration, *Centrality determination in $\sqrt{s_{NN}} = 5.02$ TeV Pb+Pb collision data in 2015*, tech. rep. ATL-COM-PHYS-2016-1287, CERN, 2016 (cit. on p. 12).
- [716]

- 717 [87] G. S. Bali, H. Neff, T. Düssel, T. Lippert and K. Schilling, *Observation of string breaking in QCD*, Phys.
 718 Rev. D **71** (11 2005) 114513, URL: <https://link.aps.org/doi/10.1103/PhysRevD.71.114513>.
- 719 [88] O. Collaboration, *Experimental properties of gluon and quark jets from a point source*, Eur. Phys. J. C
 720 **11** (1999) 217, arXiv: [hep-ex/9903027](https://arxiv.org/abs/hep-ex/9903027) [hep-ex] (cit. on p. 13).
- 721 [89] SLAC-LBL Collaboration, *Evidence for Jet Structure in Hadron Production by e^+e^- Annihilation*,
 722 Phys. Rev. Lett. **35** (1975) 1609 (cit. on p. 13).
- 723 [90] SLAC-LBL Collaboration, *Hadron Production by e^+e^- Annihilation at Center-of-mass Energies
 724 Between 2.6 GeV and 7.8 GeV*, Phys. Rev. D **26** (1982) 991 (cit. on p. 13).
- 725 [91] PLUTO Collaboration, *Jet Analysis of the $\Upsilon(9.46)$ Decay Into Charged Hadrons*, Phys. Lett. **82B**
 726 (1979) 449 (cit. on p. 13).
- 727 [92] PLUTO Collaboration, *Evidence for Gluon Bremsstrahlung in $e+e-$ Annihilations at High-Energies*,
 728 Phys. Lett. B **86** (1979) 418 (cit. on p. 13).
- 729 [93] A. H. Mueller, *Jets at LEP and HERA*, Journal of Physics G: Nuclear and Particle Physics **17**
 730 (1991) 1443, URL: <https://doi.org/10.1088%2F0954-3899%2F17%2F10%2F001> (cit. on p. 13).
- 731 [94] G. Kramer and B. Lampe, *Jet Cross-Sections in $e+e-$ Annihilation*, Fortsch. Phys. **37** (1989) 161
 732 (cit. on p. 14).
- 733 [95] T. Sjostrand, S. Mrenna and P. Z. Skands, *A Brief Introduction to PYTHIA 8.1*, Comput. Phys.
 734 Commun. **178** (2008) 852, arXiv: [0710.3820](https://arxiv.org/abs/0710.3820) [hep-ph] (cit. on p. 14).
- 735 [96] G.-Y. Qin and X.-N. Wang, *Jet quenching in high-energy heavy-ion collisions*, Int. J. Mod. Phys. E
 736 **24** (2015) 1530014, [,309(2016)], arXiv: [1511.00790](https://arxiv.org/abs/1511.00790) [hep-ph] [hep-ph] (cit. on pp. 14, 17).
- 737 [97] A. D. Martin, W. J. Stirling, R. S. Thorne and G. Watt, *Parton distributions for the LHC*, The European
 738 Physical Journal C **63** (2009) 189, ISSN: 1434-6052, URL: <https://doi.org/10.1140/epjc/s10052-009-1072-5> (cit. on p. 15).
- 740 [98] K. Olive, *Review of Particle Physics*, Chinese Physics C **40** (2016) 100001, URL: <https://doi.org/10.1088%2F1674-1137%2F40%2F10%2F100001> (cit. on p. 16).
- 742 [99] M. Hirai, S. Kumano and T.-H. Nagai, *Determination of nuclear parton distribution functions and
 743 their uncertainties at next-to-leading order*, Phys. Rev. C **76** (6 2007) 065207 (cit. on p. 15).
- 744 [100] D. de Florian and R. Sassot, *Nuclear parton distributions at next to leading order*, Phys. Rev. D **69** (7
 745 2004) 074028 (cit. on p. 15).

- 746 [101] K. Eskola, H Paukkunen and C. Salgado, *EPS09 — A new generation of NLO and LO nuclear parton
747 distribution functions*, *Journal of High Energy Physics* **2009** (2009) 065 (cit. on p. 15).
- 748 [102] S. J. Brodsky and H. J. Lu, *Shadowing and antishadowing of nuclear structure functions*, *Phys. Rev.
749 Lett.* **64** (12 1990) 1342 (cit. on p. 15).
- 750 [103] European Muon Collaboration, *The ratio of the nucleon structure functions F2N for iron and deuterium*,
751 *Physics Letters B* **123** (1983) 275 , ISSN: 0370-2693 (cit. on p. 17).
- 752 [104] O. Hen, E. Piasetzky and L. B. Weinstein, *New data strengthen the connection between short range
753 correlations and the EMC effect*, *Phys. Rev. C* **85** (4 2012) 047301 (cit. on p. 17).
- 754 [105] K. Saito and T. Uchiyama, *Effect of the Fermi Motion on Nuclear Structure Functions and the Emc
755 Effect*, *Z. Phys. A* **322** (1985) 299 (cit. on p. 17).
- 756 [106] CMS Collaboration, *Jet momentum dependence of jet quenching in PbPb collisions at sNN=2.76 TeV*,
757 *Physics Letters B* **712** (2012) 176 , ISSN: 0370-2693 (cit. on p. 17).
- 758 [107] ATLAS collaboration, *Study of inclusive jet yields in Pb+Pb collisions at $\sqrt{s_{NN}} = 5.02$ TeV*, (2017)
759 (cit. on p. 17).
- 760 [108] The CMS collaboration, *Measurement of transverse momentum relative to dijet systems in PbPb and
761 pp collisions at $\sqrt{s_{NN}} = 2.76$ TeV*, *Journal of High Energy Physics* **2016** (2016) 6, ISSN: 1029-8479,
762 URL: [https://doi.org/10.1007/JHEP01\(2016\)006](https://doi.org/10.1007/JHEP01(2016)006) (cit. on p. 17).
- 763 [109] S. Chatrchyan et al., *Jet momentum dependence of jet quenching in PbPb collisions at $\sqrt{s_{NN}} = 2.76$
764 TeV*, *Phys. Lett. B* **712** (2012) 176, arXiv: [1202.5022 \[nucl-ex\]](https://arxiv.org/abs/1202.5022) (cit. on p. 17).
- 765 [110] R. Baier, Y. Dokshitzer, A. Mueller, S. Peigné and D. Schiff, *Radiative energy loss of high energy
766 quarks and gluons in a finite-volume quark-gluon plasma*, *Nuclear Physics B* **483** (1997) 291 , ISSN:
767 0550-3213 (cit. on p. 17).
- 768 [111] M. Gyulassy, P. Levai and I. Vitev, *Jet quenching in thin quark gluon plasmas. 1. Formalism*, *Nucl.
769 Phys. B* **571** (2000) 197, arXiv: [hep-ph/9907461 \[hep-ph\]](https://arxiv.org/abs/hep-ph/9907461) (cit. on p. 17).
- 770 [112] U. A. Wiedemann, *Gluon radiation off hard quarks in a nuclear environment: Opacity expansion*, *Nucl.
771 Phys. B* **588** (2000) 303, arXiv: [hep-ph/0005129 \[hep-ph\]](https://arxiv.org/abs/hep-ph/0005129) (cit. on p. 17).
- 772 [113] P. B. Arnold, G. D. Moore and L. G. Yaffe, *Photon emission from ultrarelativistic plasmas*, *JHEP* **11**
773 (2001) 057, arXiv: [hep-ph/0109064 \[hep-ph\]](https://arxiv.org/abs/hep-ph/0109064) (cit. on p. 17).

- 774 [114] X.-F. Guo and X.-N. Wang, *Multiple scattering, parton energy loss and modified fragmentation*
 775 *functions in deeply inelastic e A scattering*, Phys. Rev. Lett. **85** (2000) 3591, arXiv: [hep-ph/0005044](#)
 776 [[hep-ph](#)] (cit. on p. 17).
- 777 [115] M. Cacciari, G. P. Salam and G. Soyez, *The Anti- $k(t)$ jet clustering algorithm*, JHEP **0804** (2008) 063,
 778 arXiv: [0802.1189](#) [[hep-ph](#)] (cit. on pp. 18, 19).
- 779 [116] S. Catani, Y. L. Dokshitzer, M. H. Seymour and B. R. Webber, *Longitudinally invariant K_t clustering*
 780 *algorithms for hadron hadron collisions*, Nucl. Phys. **B406** (1993) 187 (cit. on p. 19).
- 781 [117] Y. L. Dokshitzer, G. D. Leder, S. Moretti and B. R. Webber, *Better jet clustering algorithms*, JHEP
 782 **08** (1997) 001, arXiv: [hep-ph/9707323](#) [[hep-ph](#)] (cit. on p. 19).
- 783 [118] G. P. Salam, *Towards Jetography*, Eur. Phys. J. **C67** (2010) 637, arXiv: [0906.1833](#) [[hep-ph](#)] (cit. on
 784 p. 19).
- 785 [119] G. P. Salam and G. Soyez, *A practical seedless infrared-safe cone jet algorithm*, Journal of High Energy
 786 Physics **2007** (2007) 086 (cit. on p. 20).
- 787 [120] ATLAS Collaboration, *Measurement of the jet radius and transverse momentum dependence of*
 788 *inclusive jet suppression in lead-lead collisions at $\sqrt{s_{NN}} = 2.76$ TeV with the ATLAS detector*, Phys.
 789 Lett. **B719** (2013) 220, arXiv: [1208.1967](#) [[hep-ex](#)] (cit. on pp. 20, 39).
- 790 [121] ATLAS Collaboration, *Measurement of jet p_T correlations in Pb+Pb and pp collisions at $\sqrt{s_{NN}} = 2.76$*
 791 *TeV with the ATLAS detector*, Phys. Lett. **B774** (2017) 379, arXiv: [1706.09363](#) [[hep-ex](#)] (cit. on
 792 pp. 21–23).
- 793 [122] ATLAS Collaboration, *Measurement of the nuclear modification factor for inclusive jets in Pb+Pb*
 794 *collisions at $\sqrt{s_{NN}} = 5.02$ TeV with the ATLAS detector*, Phys. Lett. **B790** (2019) 108, arXiv:
 795 [1805.05635](#) [[nucl-ex](#)] (cit. on pp. 22, 24, 25).
- 796 [123] ATLAS Collaboration, *Measurement of jet fragmentation in Pb+Pb and pp collisions at $\sqrt{s_{NN}} = 5.02$*
 797 *TeV with the ATLAS detector*, Phys. Rev. **C98** (2018) 024908, arXiv: [1805.05424](#) [[nucl-ex](#)] (cit. on
 798 pp. 25–28).
- 799 [124] M. Spousta and B. Cole, *Interpreting single jet measurements in Pb + Pb collisions at the LHC*, Eur.
 800 Phys. J. **C 76** (2016) 50, arXiv: [1504.05169](#) [[hep-ph](#)] (cit. on pp. 26, 28, 30–32, 40).
- 801 [125] Y.-T. Chien et al., *Jet Quenching from QCD Evolution*, Phys. Rev. **D93** (2016) 074030, arXiv:
 802 [1509.02936](#) [[hep-ph](#)] (cit. on p. 26).

- 803 [126] Z.-B. Kang et al., *Inclusive production of small radius jets in heavy-ion collisions*, Phys. Lett. **B769**
 804 (2017) 242, arXiv: [1701.05839 \[hep-ph\]](#) (cit. on p. 26).
- 805 [127] J. Casalderrey-Solana et al., *A Hybrid Strong/Weak Coupling Approach to Jet Quenching*, JHEP **10**
 806 (2014) 019, arXiv: [1405.3864 \[hep-ph\]](#) (cit. on pp. 28, 36).
- 807 [128] CMS Collaboration, *Observation and studies of jet quenching in PbPb collisions at nucleon-nucleon*
 808 *center-of-mass energy = 2.76 TeV*, Phys. Rev. **C84** (2011) 024906, arXiv: [1102.1957 \[nucl-ex\]](#)
 809 (cit. on p. 29).
- 810 [129] J.-P. Blaizot, E. Iancu and Y. Mehtar-Tani, *Medium-induced QCD cascade: democratic branching and*
 811 *wave turbulence*, Phys. Rev. Lett. **111** (2013) 052001, arXiv: [1301.6102 \[hep-ph\]](#) (cit. on p. 29).
- 812 [130] J. Casalderrey-Solana, Y. Mehtar-Tani, C. A. Salgado and K. Tywoniuk, *New picture of jet quenching*
 813 *dictated by color coherence*, Phys. Lett. **B725** (2013) 357, arXiv: [1210.7765 \[hep-ph\]](#) (cit. on p. 29).
- 814 [131] R. Baier, Y. L. Dokshitzer, A. H. Mueller and D. Schiff, *Quenching of hadron spectra in media*, JHEP
 815 **09** (2001) 033, arXiv: [hep-ph/0106347 \[hep-ph\]](#) (cit. on p. 30).
- 816 [132] ATLAS Collaboration, *Measurements of the Nuclear Modification Factor for Jets in Pb+Pb Collisions*
 817 *at $\sqrt{s_{NN}} = 2.76 \text{ TeV}$ with the ATLAS Detector*, Phys. Rev. Lett. **114** (2015) 072302, arXiv: [1411.2357](#)
 818 [\[hep-ex\]](#) (cit. on pp. 32, 33).
- 819 [133] ATLAS Collaboration, *Measurement of inclusive jet charged-particle fragmentation functions in*
 820 *Pb+Pb collisions at $\sqrt{s_{NN}} = 2.76 \text{ TeV}$ with the ATLAS detector*, Phys. Lett. B **739** (2014) 320, arXiv:
 821 [1406.2979 \[hep-ex\]](#) [\[hep-ex\]](#) (cit. on p. 32).
- 822 [134] Y. Tachibana, N.-B. Chang and G.-Y. Qin, *Full jet in quark-gluon plasma with hydrodynamic medium*
 823 *response*, Phys. Rev. **C95** (2017) 044909, arXiv: [1701.07951 \[nucl-th\]](#) (cit. on pp. 33–37).
- 824 [135] CMS Collaboration, *Measurement of inclusive jet cross sections in pp and PbPb collisions at $\sqrt{s_{NN}} =$*
 825 *2.76 TeV*, Phys. Rev. C **96** (2017) 015202, arXiv: [1609.05383 \[nucl-ex\]](#) (cit. on pp. 33, 35, 36, 38,
 826 39).
- 827 [136] ALICE Collaboration, *Measurement of charged jet suppression in Pb-Pb collisions at $\sqrt{s_{NN}} = 2.76$*
 828 *TeV*, JHEP **03** (2014) 013, arXiv: [1311.0633 \[nucl-ex\]](#) (cit. on pp. 33, 39).
- 829 [137] CMS Collaboration, *Modification of jet shapes in PbPb collisions at $\sqrt{s_{NN}} = 2.76 \text{ TeV}$* , Phys. Lett.
 830 **B730** (2014) 243, arXiv: [1310.0878 \[nucl-ex\]](#) [\[nucl-ex\]](#) (cit. on pp. 37, 40).
- 831 [138] Z. Hulcher et al., *Resolution Effects in the Hybrid Strong/Weak Coupling Model*, (2017), arXiv:
 832 [1707.05245 \[hep-ph\]](#) (cit. on pp. 36, 38–40).

- 833 [139] J. Casalderrey-Solana et al., *Angular Structure of Jet Quenching Within a Hybrid Strong/Weak*
 834 *Coupling Model*, **JHEP** **03** (2017) 135, arXiv: [1609.05842 \[hep-ph\]](#) (cit. on pp. 36, 38).
- 835 [140] P. M. Chesler and K. Rajagopal, *On the Evolution of Jet Energy and Opening Angle in Strongly*
 836 *Coupled Plasma*, **JHEP** **05** (2016) 098, arXiv: [1511.07567 \[hep-th\]](#) (cit. on p. 37).
- 837 [141] P. M. Chesler and K. Rajagopal, *Jet quenching in strongly coupled plasma*, **Phys. Rev.** **D90** (2014) 025033,
 838 arXiv: [1402.6756 \[hep-th\]](#) (cit. on p. 37).
- 839 [142] P. Jacobs and X.-N. Wang, *Matter in extremis: Ultrarelativistic nuclear collisions at RHIC*, **Prog. Part.**
 840 **Nucl. Phys.** **54** (2005) 443, arXiv: [hep-ph/0405125 \[hep-ph\]](#) (cit. on p. 37).
- 841 [143] A. Majumder and M. Van Leeuwen, *The Theory and Phenomenology of Perturbative QCD Based Jet*
 842 *Quenching*, **Prog. Part. Nucl. Phys.** **66** (2011) 41, arXiv: [1002.2206 \[hep-ph\]](#) (cit. on p. 37).
- 843 [144] J. Casalderrey-Solana, H. Liu, D. Mateos, K. Rajagopal and U. A. Wiedemann, *Gauge/String Duality,*
 844 *Hot QCD and Heavy Ion Collisions*, (2011), arXiv: [1101.0618 \[hep-th\]](#) (cit. on p. 37).
- 845 [145] J. Casalderrey-Solana, J. G. Milhano and P. Quiroga-Arias, *Out of Medium Fragmentation from*
 846 *Long-Lived Jet Showers*, **Phys. Lett.** **B710** (2012) 175, arXiv: [1111.0310 \[hep-ph\]](#) (cit. on p. 37).
- 847 [146] T. Hirano, P. Huovinen and Y. Nara, *Elliptic flow in Pb+Pb collisions at $\sqrt{s_{NN}} = 2.76 \text{ TeV}$: hybrid*
 848 *model assessment of the first data*, **Phys. Rev.** **C84** (2011) 011901, arXiv: [1012.3955 \[nucl-th\]](#)
 849 (cit. on p. 38).
- 850 [147] J. Rusnak, *Inclusive spectrum of charged jets in central Au+Au collisions at $\sqrt{s_{NN}} = 200 \text{ GeV}$ by*
 851 *STAR*, **PoS EPS-HEP2013** (2013) 191 (cit. on p. 39).
- 852 [148] CMS Collaboration, *Measurement of jet fragmentation in PbPb and pp collisions at $\sqrt{s_{NN}} = 2.76$*
 853 *TeV*, **Phys. Rev. C** **90** (2014) 024908, arXiv: [1406.0932\[nucl-ex\] \[nucl-ex\]](#) (cit. on p. 40).